Design and Optimization of Low-Specific Speed Centrifugal Pump

by

Muhammad Fasahat Khan

A thesis
presented to the University of Waterloo
in fulfillment of the
thesis requirement for the degree of
Masters of Applied Science
in
Mechanical and Mechatronics Engineering

Waterloo, Ontario, Canada, 2023

Author's Declaration

I hereby declare that I am the sole author of this thesis. This is a true copy of the thesis, including any required final revisions, as accepted by my examiners.

I understand that my thesis may be made electronically available to the public.

Abstract

Centrifugal pumps find applications in a wide range of industries, such as rocketry, oil and gas, petroleum, etc. A main property used to characterize the design of pumps is the specific speed, which relates the flow properties of the pump at its operating point. Pumps in the low-specific speed range have been of particular interest. These are characterized by the high head value (representative of mechanical energy) produced at a relatively low flow rate. A lower flow rate reduces the power requirements required to operate the shaft that rotates the impeller. However, the design of such pumps presents many challenges. Most of the existing design methodologies are developed for pumps in a normal specific speed range–low specific-speed pumps fall out of this range. These methods, when applied for the design of low-specific speed pumps, can result in dimensions that are not physically realizable. The work done herein combines empirical relations based on experimental measurements and theory for the optimal design of a low-specific speed pump. This is done by delineating a baseline design for the design flow rate of 253 USGPM based on these relations and then optimizing the baseline design based on its performance features obtained using numerical simulations. Each design was simulated with both a tangential diffuser and an axial diffuser to assess the impact of these diffuser options on performance characteristics.

The performance of the designs are evaluated in terms of the steepness of the head-capacity curves, the efficiency, and the power requirements. The steepness of the head-capacity curve refers to the difference between the head value near the shut-off point (no flow rate) and that at the Best Efficiency Point (BEP), *i.e.*, the flow rate at which the pump operates with maximum efficiency. It is a desirable feature, since it broadens the range of head delivered with changes in flow rate. Another desirable characteristic of the pump is to have its BEP in close proximity to the design flow rate, so that the efficiency of the operating point of the pump is close to its maximum efficiency. The numerical simulation involved the solution of Reynolds Averaged Navier-Stokes (RANS) equations using SST $k - \omega$ model.

The designs with a tangential volute were first simulated. The performance features obtained for the baseline design had some undesirable features, which include slight instability (positive slope) in the head-capacity curve near the shut-off point and the BEP being located at a much higher discharge than the design flow rate. These issues were resolved with the throat area of the volute being reduced by 50% (referred to as first iteration design), which made the head-capacity curve much steeper and also shifted the BEP a lot closer to the design flow rate (a difference of about 100 USGPM between the BEP and the design flow rate as opposed to the difference of about 400 USGPM observed for the

baseline case). The reduction in the volute throat also increased the efficiency of the design point by about 13% and reduced the power requirements compared to those of the baseline design for the flow rate up to approximately 500 USGPM. Power requirements for flow rates greater than 500 USGPM were about the same for both designs. The head delivered at the design point was about the same for both cases. Even further improvement was obtained when the gap width of the volute was reduced by 50% in addition to volute throat reduction (referred to as the second iteration design). This resulted in the head-capacity curve being shifted vertically upwards, *i.e.* the head delivered increased for all flow rates by almost the same margin compared to that delivered from the first iteration design. At the design point, the head delivered increased from 96.66 m for the first iteration design to 98.04 m for the second iteration design. The efficiency also improved by 2.34%. However, no significant changes were observed in the power requirements.

The same design iterations were simulated for the case of an axial diffuser. Although no difference in performance characteristics was observed under partload and design conditions between the two corresponding designs, the head delivered and efficiency noticeably decreased at overload conditions. Overall, the design with tangential volute performed better.

Another design simulated involved a radial bladed impeller with tangential volute. The head delivered at the design point for this case increased to more than 120 m. However, this came at the cost of a significant instability observed at partload conditions. Additionally, the power requirements also increased substantially in this case.

Acknowledgements

It's been said that nothing worth doing can be done alone. This project was certainly worth doing, and hence, it couldn't have been done all by myself. First and foremost, I would like to extend my sincere gratitude to my supervisor, Jean-Pierre Hickey, who went above and beyond his duties as a supervisor in ensuring successful completion of my Masters. I am also grateful to Tim Gjernes for the many precise suggestions and feedback he gave over the course of the project. His expertise in pumps was instrumental at every stage of the project. The knowledge and insights shared by Nicholas Guenther were also helpful.

It would be unfair not to mention Radek Maca of CFD Support who responded promptly to resolve any technical issues we had with the simulation software.

Lastly, I am also thankful to my family and friends, most of whom have never been reluctant to help me in whatever way possible whenever I have reached out to them in the past three years.

Dedication

This is dedicated to my mother.

Table of Contents

Author's Declaration ii

Abstract iii

Acknowledgements v

Dedication vi

List of Figures x

List of Tables xiii

1 Introduction 1

1.1 Motivation and Objectives 3

1.2 Organization of the Thesis 5

1.3 Contributions of the Research 5

2 Literature Review 6

2.1 Flow Physics 6

2.2 Effect of Design Variables on Performance Features 7

2.3 Unconventional Design Methods 9

2.3.1 Radial bladed Impeller 10

2.3.2 Other Unconventional Methods 10

3 Theory and Design Methodology **12**
3.1 Basic Definitions . . . 12
3.2 Design Methodology . . . 15
3.2.1 Impeller Design . . . 15
3.2.1.1 Meridional Section . . . 15
3.2.1.2 Blade . . . 18
3.2.2 Volute Design . . . 25
3.3 Numerical Model . . . 27

4 Results and Analysis **29**
4.1 Grid Independency Results . . . 29
4.2 Performance Features of Baseline Design . . . 31
4.3 First Design Iteration . . . 31
4.3.1 Effect of Throat Area Reduction on the Internal Flow Field . . . 33
4.4 Second Design Iteration . . . 37
4.4.1 Effect of Gap Width Reduction on the Internal Flow Field . . . 38
4.5 Volute with Axial Diffuser . . . 40
4.6 Radial Bladed Impeller . . . 45

5 Conclusions and Recommendations **50**

References **53**

APPENDICES **58**

A Python Code for development of Parametric Model of Pump **59**

B Turbulence Models **71**
B.1 k-ε Model . . . 71
B.2 k-ω Model . . . 72
B.3 SST k-ω Model . . . 72

C Mesh used for Numerical Simulations 74

List of Figures

1.1 Typical arrangement of a single-stage, centrifugal pump. Source: [31] . . . 2

1.2 Front view and meridional view of a radial impeller. LE: Leading Edge, TE: Trailing Edge. Source: [18] . . . 2

1.3 Cross-sectional view of a conventionally designed volute from front (modified from [18]). . . . 3

3.1 Meridional view of the pump with arrows showing direction of leakage flow (modified from [18]) . . . 14

3.2 Meridional view of the impeller with dimensions . . . 16

3.3 Velocity triangle at impeller inlet. c_1: Fluid absolute velocity, c_{1m}: Meridional component of fluid velocity, i_1: Blade incidence angle, u_1: Rotational velocity of impeller, w_1: Fluid relative velocity, $\beta_{1'}$:Angle of relative velocity vector to u_1, β_1: Blade inlet angle. . . . 19

3.4 Blade incidence causing flow separation at blade leading edge (source: [18]). 20

3.5 Illustration of slip phenomenon with flow streamlines deviating towards the blade pressure side beyond the solid vertical line [18]. . . . 21

3.6 Velocity triangle at impeller outlet. The dashed lines represent the blade-congruent flow, while the actual flow is represented by the solid lines. The superscript ' represents the flow quantities with blade blockage effects taken into account. γ: Slip factor, δ: Deviation angle. [18] . . . 22

3.7 Circular arc method for the design of blade. β_1: Blade inlet Angle, β_2: Blade outlet angle, A: Point of trailing edge, B: Construction point for line AE, E: Point of leading edge, M: Center of the arc, R: Radius of the arc. (source: [34]) . . . 25

3.8 Empirical design constants for the volute (source: [38]) 26

4.1 Grid convergence study at the design flow rate 30
4.2 Performance characteristics of the baseline design 32
4.3 Performance characteristics resulting from reduction in volute throat area of the baseline design in comparison to those of the baseline design 33
4.4 Pressure distribution in Pascals over the blade height at 100 USGPM. Point 0 corresponds to the shroud and point 1 corresponds to the hub of the impeller. 35
4.5 Distribution of total pressure (mechanical energy) in the pump for (a) Baseline at 400 USGPM, (b) First iteration design at 400 USGPM, (c) Baseline at 600 USGPM, and (d) First iteration design 600 USGPM. 36
4.6 Distribution of Turbulent Kinetic Energy (TKE) at the flow rate of 600 USGPM for (a) Baseline design and (b) First iteration design. 37
4.7 (a) Head delivered from the impeller and (b) Head loss in volute for the two designs 38
4.8 Cavitation in the two designs expressed as (a) NPSH (m) and (b) Cavitating volume (%) 39
4.9 Performance characteristics resulting from reduction in volute throat area and gap width of the baseline design in comparison to those of the first iteration design 40
4.10 (a) Head delivered from the impeller and (b) Head loss in volute for the two designs 41
4.11 (a) Pump with tangential volute and (b) Pump with axial volute 42
4.12 Performance characteristics of the baseline design with axial volute in comparison to those of the same design with tangential volute 43
4.13 Performance characteristics of the first iteration design with axial volute in comparison to those of the same design with tangential volute 44
4.14 A typical design of a double-acting impeller (source: [38]) 46
4.15 Performance characteristics of the radial bladed impeller with tangential volute 47
4.16 Pressure distribution in Pascals over the pressure and suction sides of the blade in streamwise direction at a discharge rate of (a) 100 USGPM, (b) 253 USGPM, (c) 400 USGPM, and (d) 600 USGPM. 49

C.1 Mesh refinement at the impeller inlet 74
C.2 Mesh refinement at the impeller outlet 75
C.3 Mesh for the impeller 76
C.4 Mesh refinement near the tongue of the volute 77
C.5 Mesh for the volute 78

List of Tables

3.1 Design values defining the meridional section of the impeller 18
3.2 Design values defining the blade of the impeller 24

4.1 Performance characteristics of the three designs at the operating point . . 39

Chapter 1

Introduction

Centrifugal pumps are turbomachines that find applications in a wide range of industries. They are used for transporting liquids by raising their mechanical energy level through hydraulic processes involving centrifugal force, and hence, the name. The process uses a shaft rotating at some specified frequency to pump a liquid with a certain flow rate. All centrifugal pumps consist of at least an inlet, one impeller and a collector where most of the kinetic energy at the impeller outlet is converted into static pressure.

Depending on the application, different types of impellers and volute casings can be used to build different types of pumps. The pump can use several impellers operating in series, in which case it is referred to as a multi-stage pump. In its simplest form, a centrifugal pump consists of an inlet, an impeller mounted on a shaft, and a volute casing. Figure 1.1 shows a typical arrangement of the centrifugal pump with labelled components. The impeller shown in the figure is conventionally designed with backward bent blades. The arrows in the figure represent the flow direction.

An impeller is a significant component of the pump that is characterized by shroud (front cover), hub (back cover), and blades that impart energy to the fluid. An impeller with both the shroud and hub built into it is often referred to as a closed impeller. In some cases, the shroud is not built into the impeller, in which case it is referred to as a semi-open impeller. A detailed view of an impeller is shown in Figure 1.2.

Figure 1.2 shows the direction of rotation of the impeller. The blade edge near the inflow is defined as the Leading Edge (LE), while the edge near outflow is named the Trailing Edge (TE). The side of the blade that experiences the highest pressure from the fluid is referred to as the Pressure Side (PS), while the other side that experiences the

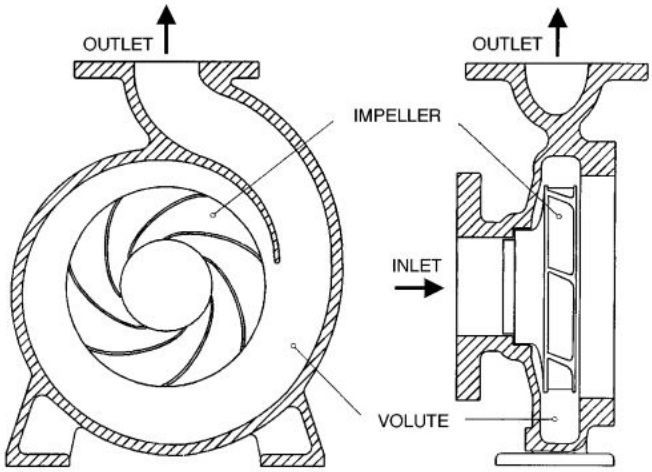

Figure 1.1: Typical arrangement of a single-stage, centrifugal pump. Source: [31]

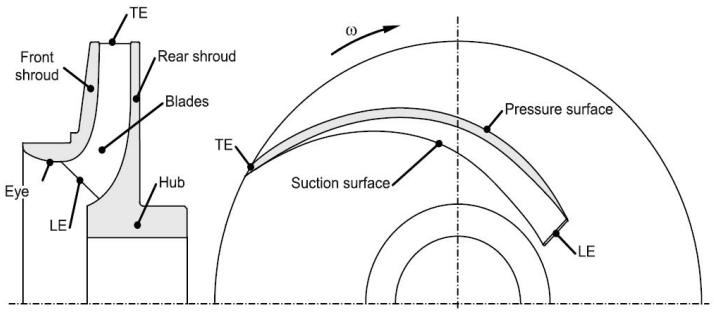

Figure 1.2: Front view and meridional view of a radial impeller. LE: Leading Edge, TE: Trailing Edge. Source: [18]

lower pressure is called the Suction Side (SS). The flow discharged from the impeller is collected in volute.

The volute is another significant component of the pump. A conventionally designed volute is asymmetric and is shaped like a spiral, as shown in Figure 1.3. The diameter D_3 defines the radial position of the tongue. The radial distance $(D_3 - D_2)/2$ is a critical parameter, referred to as gap width. This parameter largely defines the rotor-stator interaction and strongly influences the radial force experienced by the impeller. The throat area is the interface where the spiral volute meets the outlet. It is located directly above the volute tongue.

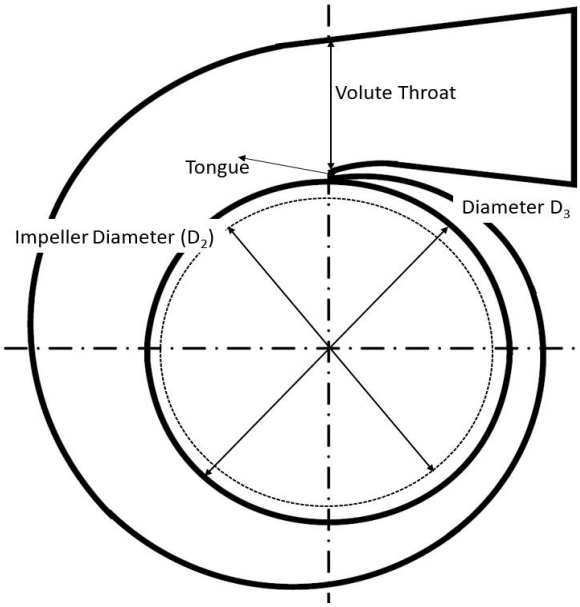

Figure 1.3: Cross-sectional view of a conventionally designed volute from front (modified from [18]).

1.1 Motivation and Objectives

When designing pumps, an important parameter that is used to guide the design process is the specific speed of the pump. It relates the flow variables of the pump at its operating point. A wide range of specific speeds for pumps, depending on the application. Of these, pumps in the low-specific speed range are of particular importance. These are characterized

by high head (representative of mechanical energy) produced at a low flow rate and find applications in a wide range of industries, including oil and gas, and chemical. However, design of centrifugal pumps in low specific speed range presents many challenges.

First, the disk friction losses for low-specific speed centrifugal pumps are high and increase exponentially as the specific speed decreases [38]. This significantly reduces the efficiencies of centrifugal pumps in a low-specific speed range. The disk friction is proportional to the third power of the speed and the fifth power of the diameter [18]. An increase of the diameter raises the energy imparted to the fluid at impeller outlet, but comes at a huge cost of a significant increase in friction losses. This trade-off is a limiting factor in the design of low-specific speed centrifugal pumps.

In addition, pump stability is also an important consideration for low specific speed centrifgual pumps. The stability criterion is violated if the slope of the head capacity curve is positive ($\frac{dH}{dQ} > 0$) [17]. Gulich [18] relates the stability of the pump to its specific speed, where low specific speed centrifugal pumps are found to be more prone to unstable head capacity characteristics. On the same note, an important performance feature of the pump is the steepness of the head-capacity curve, *i.e.* the difference between the head value near the shut-off point and that at the Best Efficiency Point (BEP). Although it is important to have a continuously rising head-capacity curve with the decrease in capacity, maximizing the steepness can be beneficial to widen the operating range of the pump. This is particularly important when handling slurry as, in this case, the head tends to change very little with the change in flow rate.

In addition, conventional design approaches are developed for the normal specific speed range, and low-specific speed pumps often fall outside of this range. These approaches result in unrealistic dimensions, such as extra ordinarily small hydraulic passages, when used for the design of low-specific speed centrifugal pumps. This explains the importance of Computational Fluid Dynamics (CFD) for the design of low-specific speed centrifugal pumps, which can be used to explore different options in the design space to locate the ideal candidate with improved performance features.

A different pumping system may be more appropriate for low-specific-speed applications, such as positive displacement pumps. Another option is to use multistage pumps, with several impellers operating in series and guide vanes installed to guide the flow from one impeller in series to the next. These can generate relatively high head with each impeller contributing to an increase in the head value. However, when pumping liquids that are corrosive and contain solid particles, such as slurry, the parts of the pumping system may easily wear out. Multistage pumps, for example, can be very difficult to use because they have many parts that can wear out, significantly reducing the lifespan of the pump.

Centrifugal pumps are more robust in this regard and have fewer parts to wear out.

This work attempts to present a design methodology based on analytical and empirical relations for the design of centrifugal pumps in the low-specific speed range. The methodology is complemented by steady-state numerical simulations that are used to obtain the performance characteristics of the design and explore the design space using results from the literature to locate a design candidate with improved performance features. The internal flow fields are analyzed to better understand the impact of changes made to the geometry. The performance characteristics of concern are the stability of head-capacity curve, efficiency at BEP, and the steepness of the head-capacity curve.

1.2 Organization of the Thesis

The work is divided into 4 main chapters. Chapter 2 presents a summary of the literature related to design considerations and optimization of centrifugal pumps. Chapter 3 outlines the design methodology used to delineate the impeller and volute of the centrifugal pump. Moving on, Chapter 4 presents the performance characteristics of the design created using the methodology presented in Chapter 3, named Baseline Design. It further explains the modifications made to the Baseline Design and how the changes led to improved performance features for the final design. Finally, Chapter 5 summarizes the main findings of the work and recommendations for future potential work.

1.3 Contributions of the Research

Most of the work done for the project can be divided into the following three aspects:

- Design strategy based on theory and empirical relations for low-specific speed centrifugal pump
- Impact of the volute shape and geometry on the performance features of the pump
- Development of a parametric model based on design variables for the pump

Chapter 2

Literature Review

As discussed in Chapter 1, the design of centrifugal pumps in low-specific speed range presents many challenges. Efforts have been made to better understand these issues by analyzing internal flow fields under different working conditions through experimental investigations and numerical simulations. Parametric studies have also been performed to understand the effect of different design variables on performance characteristics. In addition to conventional design approaches, unconventional designs have been employed in the literature which have been shown to mitigate the performance issues of low-specific speed centrifugal pumps. Parametric studies are better handled through the use of optimization algorithms, which can be coupled with CFD to explore the design space for an ideal candidate that optimizes an objective function or a set of objective functions. These aspects of the literature are discussed in detail in subsequent sections.

2.1 Flow Physics

The internal flow field of a centrifugal pump is governed by complex flow features resulting from rotor-stator interactions. The internal flow field and the resulting flow structures vary with different flow rates. For example, the flow separation phenomenon in impeller passages is most intense at underload (flow rate lower than design flow rate) conditions [7, 47]. Experimental investigations by Zhang et al. show that the uniformity of streamlines in impeller passages at midspan becomes distorted at underload and large-scale vortex structures develop [48, 47]. Large-scale vortex structures result in reverse flow regions (regions where flow is directed towards the impeller inlet) that occupy most of the impeller channels at underload [15, 48, 47]. It implies that not all the fluid from the impeller is

collected in the volute at underload. Some of the fluid discharged re-enters the impeller channels. On the other hand, no reverse flow is observed for design flow rate and overload (flow rate higher than the design flow rate) conditions [15, 48, 47]. At underload, flow tends to concentrate primarily toward the blade pressure side, where higher velocity regions are observed compared to those observed on the blade suction side [15, 48, 47]. On the other hand, at overload conditions, flow tends to concentrate mostly on the blade suction side [15, 23, 48, 47]. At the design flow rate, the flow distribution is relatively uniform, especially towards the impeller outlet [15, 48, 47]. However, small-scale flow separation within impeller passages can occur even at the design flow rate [15, 48, 47]. Differences between flow distributions at overload and underload conditions manifest themselves in the form of differences between flow structures and their evolution in the pump.

The flow distributions at the design flow rate and underload working conditions result in jet-wake flow pattern towards the impeller outlet [7, 23, 47]. An overview of jet-wake structures in centrifugal pumps is given in [32]. The results of the experimental findings show that the jet-wake pattern is more pronounced at underload and design flow rate and decreases at overload [42, 47]. The flow pattern at the impeller outlet results in unsteady vortex shedding from the trailing edges of the blade. Zhang et al. used experimental investigations to study different vortical structures and their evolution in a low specific speed centrifugal pump and showed that not only these structures are different under different working conditions (underload versus overload), but also they show significant spatial variations within the pump geometry [48, 47]. These structures also evolve differently. For example, the experimental results show that there is a positive vorticity sheet and a negative vorticity sheet that is generated at the blade outlet at the design flow rate [47]. For the blade that is in close proximity to the tongue, the positive sheet is transported and cut through the volute tongue, but the negative sheet has no impinging effect [47]. These flow structures have been shown to have a direct correlation with the pressure pulsation energy at the impeller periphery, which has been shown to exhibit spatial variations as well as variations with different working conditions (underload versus overload) [15, 48].

2.2 Effect of Design Variables on Performance Features

Several parametric studies have been done to investigate the influence of different impeller design variables on performance characteristics. Cui et al. investigated the performance features of low-specific speed centrifugal pumps with two different blade outlet angles through experimental and numerical investigations [12]. Higher blade outlet angle resulted

in higher static and total pressure at the impeller outlet at the design flow rate, while also improving discharge capacity and efficiency [12]. Gao et al. investigated the influence of the blade trailing edge profile on the performance characteristics of low-specific speed centrifugal pumps [16]. Numerical simulations showed that the EBS (Ellipse on Both Sides of the edge) and EPS (Ellipse on Pressure Side) profiles, in comparison to blunt profile, have a positive influence on the efficiency of the pump, while also reducing the amplitudes of pressure pulsations at the impeller-volute interface [16]. Pressure pulsations can also be reduced by slightly trimming the impeller (reducing the outer diameter of the impeller) [18]. However, excessive impeller trimming can significantly alter geometric and kinematic similarity conditions, resulting in internal flow recirculation that can significantly lower pump head and efficiency [36]. Some studies suggest that the impeller trimming should not exceed more than 25% of the initial impeller diameter [4, 29, 36].

Another important design variable relevant for semi-open impellers is the tip clearance, *i.e.* the gap between the tip of the blade and the front casing cover. Pump performance characteristics have been shown to improve as the tip clearance decreases and worsen as it increases [5, 11]. The effect is more pronounced for the low-specific speed pump [5]. Semi-open impeller can help improve efficiency by reducing disk friction, but this comes at the cost of strong leakage flow/secondary flow through tip clearance[11]. This effect can be mitigated by reducing the tip clearance. Design variables are an important consideration not only for performance features (head, efficiency, and power requirements), but they can also have a profound effect on cavitation.

Cavitation refers to the development of vapor bubbles as the static pressure of the liquid falls below the saturated vapor pressure due to excess local velocities and flow separation. These bubbles are transported downstream where they implode (condense suddenly) once the static pressure exceeds the vapor pressure. Although not the main focus of this project, excessive cavitation can severely impair pump performance characteristics (head and efficiency) of the pump accompanied by noise, vibrations, and material damage [18]. Cavitation is mainly influenced by the impeller geometry at the inlet, such as the inlet diameter and the blade leading edge profile. This is usually where the static pressure is lowest in the entire domain. Balasubramanian et al. investigated the effect of different leading edge profiles on cavitation behaviour of the pump using experimental and numerical investigations [2]. The results indicated that parabolic profiles are the best to minimize cavitation damage, followed by elliptical and circular profiles, while blunt profiles are the worst [2]. Similar research was done by Tao et al., who showed a wider low pressure region exists near the blade leading edge for blunt profiles in comparison to that observed for circular and elliptical profiles [39]. This should be expected since an abrupt geometry change for blunt profiles gives rise to flow separation, which significantly lowers the static

pressure.

Studies have also been conducted to examine the influence of volute design variables on the performance of centrifugal pumps. Kurokawa et al. suggested that optimization of volute design parameters is important to improve the efficiency of low-specific speed centrifugal pumps [26]. Enlargement of the volute throat area has been shown to have an important influence on the performance of low-specific speed centrifugal pumps by displacing the BEP to a higher flow rate and flattening the head-capacity curve [10, 46]. Research also reveals that the radial gap between the impeller outlet and the tongue is a significant parameter [26, 46]. The gap, when reduced, can improve the pump efficiency [26, 46]. A potential risk of reducing this radial gap is related to noise and vibrations that result from intense pressure fluctuations. However, Kurokawa et al. showed that pressure fluctuations do not change significantly with decreasing radial gap for the case of low-specific speed centrifugal pumps [26].

There are two methods commonly employed for volute design. Stephanoff method is the constant velocity method where the volute is developed so that the circumferential velocity stays the same at all cross-sections [38], while Pfleiderer method is based on constant angular moment at all cross-sections [33]. Alemi et al. compared the performance features of the two low-specific speed centrifugal pumps, one with the volute designed using the Stephanoff method and the other with the volute designed using the Pfleiderer method [1]. Pfleiderer method resulted in slightly higher head and efficiency at low capacity, while the Stephanoff method gave slightly better results at the design flow rate [1]. At higher capacity, the Stephanoff method resulted in far better performance characteristics than those of the Pfleiderer method [1]. The Stephanoff method has the additional advantage of resulting in a lower radial force experienced by the impeller at the design point and low capacity [1]. This is to be expected since constant velocity ensures the uniformity of static pressure around the impeller periphery.

2.3 Unconventional Design Methods

As mentioned above, unconventional design approaches have been employed in the literature to mitigate the performance issues of the low-specific speed pump. A common unconventional design that was developed to cater for low-specific speed applications involves a radial bladed impeller.

2.3.1 Radial bladed Impeller

The literature reveals that one of the first investigations on the topic of low-specific speed centrifugal pumps was carried out by Barske [3, 13]. Barske proposed a semi-open impeller with radial vanes as a favorable design for low-specific speed hydraulics [3]. Radial blades are particularly favorable for low-specific speed applications. This design has a relatively high blade outlet angle of 90°and radial blades allow space for a greater number of blades than that used in a conventional design with backward bent blades. As will be shown, both of these factors (blade outlet angle and number of blades) are directly related to the head produced by the impeller and contribute to significantly increasing the head output. Dahl performed a parametric study of the design proposed by Barske [13]. Dahl [13] showed that a radial bladed impeller gives a higher head over the entire flow range compared to a conventionally designed impeller with only a 1.5% decrease in efficiency at BEP. However, the improved performance for the radial bladed impeller came at a cost of significant instability observed in head-capacity characteristics. The semi-open impeller has the additional drawback of experiencing increased axial thrust due to the pressure difference between the front and back sides of the impeller. However, Dahl [13] showed that both of these issues can be circumvented by using balance holes in the semi-open impeller.

2.3.2 Other Unconventional Methods

Other unconventional designs have been investigated for low-specific speed applications. Satoh et al. investigated a palm-sized pump with an impeller designed as a disk with ditches used as flow passages and many shallow grooves etched into the surface near the periphery of the disk [35]. The design was shown to have satisfactory performance characteristics [35]. Kagawa et al. proposed a J-groove pump with a circular casing and a disk with many J-shaped shallow grooves on either side for low-specific speed applications. The pump was shown to have stable head-capacity characteristics and higher head output than conventional design options over the entire flow range through experimental investigations [20]. Klas et al. investigated the performance characteristics of a low-specific speed pump with an impeller with wide trailing edges and recirculation channels built into these edges [25]. The performance characteristics of pumps with different shapes of recirculation channels were analyzed and the results indicated that L-shaped and T-shaped channels had a positive influence on the efficiency and head curve stability, respectively. [25]. Olimstad et al. used experimental investigations and CFD to iterate on design candidates for low specific speed applications and investigated the characteristics of an impeller with S-

shaped blades, which was found to give greater head output and higher efficiency than the other design candidates [30]. Another unconventional design approach commonly used for low-specific speed hydraulics is the addition of splitter blades in the impeller. Chabannes et al. investigated the effect of splitter blades on the performance characteristics of the low-specific speed pump [9]. Although head output was found to increase, the BEP was displaced further to the right and the head-capacity curve became flatter with the addition of splitters [9]. Wei et al. investigated the influence of the width of the drainage gap built into the impeller blades on the performance characteristics of low-specific speed pumps using experimental and numerical investigations [41]. Although the 1.5 mm gap width resulted in an increase in efficiency with the head remaining essentially the same, the head appeared to drop significantly with only a slight increase in efficiency when the gap width increased to 6 mm [41]. Kim et al. proposed a method for the design of impellers based on empirical relations for design variables for low-specific speed centrifugal pumps to be used for small liquid rocket engines and compared the performance characteristics of the design obtained with those of the design obtained using the conventional method [24].

Chapter 3

Theory and Design Methodology

This chapter outlines the definitions of quantities that define the performance features of the pump. This is followed by the methodology used to determine the dimensions of the baseline design of the centrifugal pump. The baseline design refers to the zeroth iteration, whose performance characteristics can be evaluated using CFD and used as a basis for further improvement through multiple design iterations. The strategy consists of a simplified theory based on velocity triangles and statistical correlations. The baseline dimensions are then outlined, which is followed by a detailed description of the numerical scheme used for CFD simulations.

3.1 Basic Definitions

A fundamental measure of pump performance is the total head, which is generated by the impeller [38]. It quantifies the change in mechanical energy of the fluid after it goes through the pump. The mechanical energy per unit volume of the fluid is represented as the total pressure, p^T. In most cases, the change in the potential energy of the fluid through the pump is negligible compared to the change in kinetic energy [7], and therefore the total pressure is defined according to equation (3.1).

$$p^T = p + \frac{1}{2}\rho v^2 \tag{3.1}$$

where ρ is the density of the medium, p is the pressure, and v is the velocity magnitude. The head delivered is estimated according to:

$$H = \frac{p_2^T - p_1^T}{\rho g} \tag{3.2}$$

where p_2^T is the average value of the total pressure measured at the outlet, p_1^T is the average value measured at the inlet of the pump, and g is the gravitational constant. The head delivered determines the overall efficiency, η^{pump}, which is estimated according to:

$$\eta^{pump} = \frac{\dot{V}_2 h_2 - \dot{V}_1 h_1}{M\omega} \tag{3.3}$$

where $\dot{V}$ is the volumetric flow rate, M is the torque, ω is the angular velocity, and h is the specific enthalpy. The overall efficiency is the product of the mechanical efficiency, η^m, volumetric efficiency, η^v, and hydraulic efficiency, η^h [38].

Mechanical efficiency is related to the power loss in bearings and disc friction. It is calculated as the ratio of the power gained by the impeller to the power applied to the pump shaft [38]. Volumetric efficiency, on the other hand, is related to the loss of flow as leakage through sidewall clearances between the impeller and casing. The loss due to leakage flow is illustrated in Figure 3.1, where the arrows indicate the direction of leakage flow. Therefore, the flow output at the pump outlet is less than the flow discharged from the impeller by the amount of leakage, and the ratio of flow rate at outlet to flow rate at the inlet of the pump is referred to as volumetric efficiency. Lastly, hydraulic efficiency quantifies the hydraulic losses of the pumping fluid that decrease the head delivered by the impeller. It is the ratio of the head measured at the outlet to the maximum head that can be delivered by the impeller. The principle of conservation of angular momentum can be used to derive the theoretical/maximum head, H_{th}, that can be delivered assuming no hydraulic losses, which is given as [38]:

$$H_{th} = \frac{u_2 c_{2u} - u_1 c_{1u}}{g} \tag{3.4}$$

where, u_2, is the rotational velocity of the impeller at its outer diameter, u_1 is the rotational velocity of the impeller at its inlet, c_{2u} is the tangential component of fluid velocity at the impeller outlet, and c_{1u} is the tangential component of the fluid velocity at the inlet. Equation (3.4) is also known as the Euler head equation. One factor that can have a negative impact on the delivered head, and hence on hydraulic efficiency, is excessive cavitation.

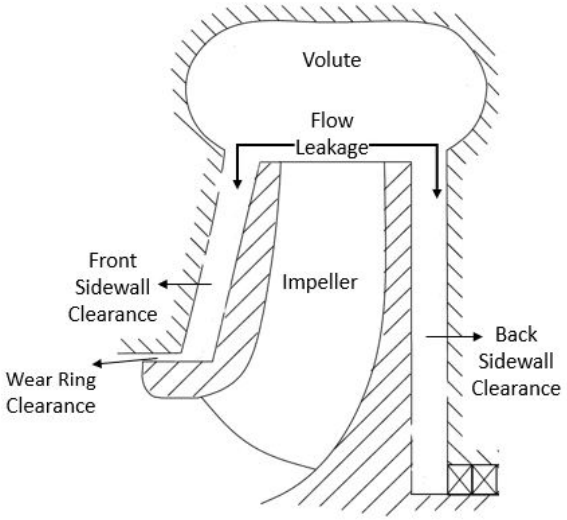

Figure 3.1: Meridional view of the pump with arrows showing direction of leakage flow (modified from [18])

There are several ways to quantify cavitation. One is through Net Positive Suction Head (NPSH), which is estimated as the difference between the head value and the saturated vapor pressure at the impeller inlet according to the following:

$$NPSH = \frac{p_{in} + \frac{1}{2}\rho u_{in}^2 - p_V}{\rho g} \tag{3.5}$$

In equation (3.5), the subscript 'in' is used to denote impeller inlet, and p_V is the saturated vapor pressure. The term evaluated using equation (3.5) is also referred to as available NPSH, or NPSH_A. Another similar quantity is defined as the required NPSH, or NPSH_R, which is a measure of minimum NPSH required to avoid the inception of cavitation. Cavitation can also be quantified as cavitation index, σ, which is calculated according to:

$$\sigma = \frac{p_{in} - p_V}{\frac{1}{2}\rho u_{in}^2} \tag{3.6}$$

The desired output from the pump in terms of the head delivered at a given flow rate and rotor speed defines the specific speed of the pump. Unfortunately, there are various ways in the literature to calculate this quantity [18]. For most purposes here, the specific

speed, n_q, is calculated according to:

$$n_q = \frac{n\sqrt{Q_{opt}}}{H_{opt}^{0.75}} \tag{3.7}$$

where n is the rotor speed in RPM (Revolutions Per Minute), Q_{opt} is the flow rate through the pump at its operating point in m^3/s, and H_{opt} is the head required at this point in m. A pump is generally considered to have low specific speed if $n_q < 20$ [18]. The operating point defined by Q_{opt} and H_{opt} is often referred to as the design point. Normally, turbomachines are designed to have their highest efficiency at the design point [7], as the pump is designed to operate at this point. The design point, defined by the specific speed, is used as a starting point for the pump baseline design.

3.2 Design Methodology

The methodology for the baseline design depends on the specific speed. The pump is designed to deliver a head of 272 ft at a flow rate of 253 USGPM (US Gallons Per Minute) with a rotor speed of 1750 RPM. These dimensions characterize the main design features of the pump. Converted to SI units, these quantities yield a specific speed of around nine, according to equation (3.7). This value is used as a basis for both the impeller and volute design.

3.2.1 Impeller Design

The design of the impeller can be divided into two parts: the design of the meridional section and the design of the blade. The meridional section is designed based on empirical relations, most of which are sourced from Gulich [18]. These empirical relations are derived from experimental measurements of the performance characteristics of a number of pumps of various sizes [18].

3.2.1.1 Meridional Section

The meridional section of the impeller, with all relevant dimensions, is shown in Figure 3.2. The leading and trailing edges of the blades are not shown to avoid cluttering the image.

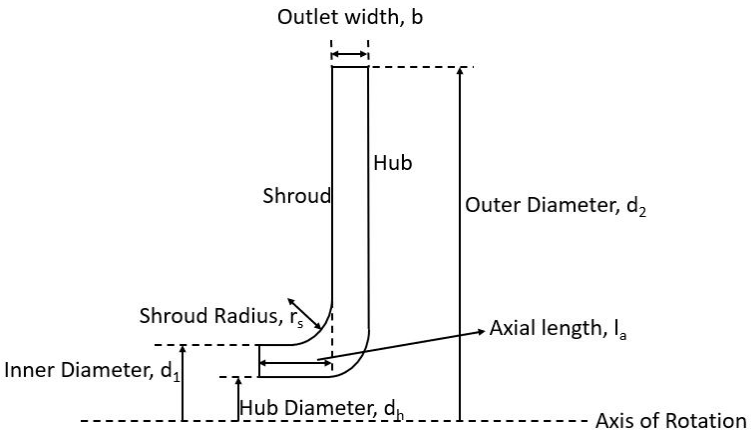

Figure 3.2: Meridional view of the impeller with dimensions

Of the dimensions shown in Figure 3.2, the outer diameter of the impeller was first established using an empirical relation that is based on the head coefficient. The head coefficient, ψ, is a non-dimensional measure of the head, defined according to equation (3.8).

$$\psi = 2g\frac{H}{u_2^2} \tag{3.8}$$

Gulich [18] published an empirical relationship between head coefficient and specific speed based on experimental measurements, which is defined according to:

$$\psi_{opt} = 1.21e^{-0.77n_q/n_{q,ref}} \tag{3.9}$$

where $n_{q,ref}$ is the reference measure of the specific speed taken to be 100 (a value which is empirically determined in the literature). With an estimate of the head coefficient, the outer diameter of the impeller, d_2, was established based on another empirical relation from[18] defined according to equation (3.10).

$$d_2 = \frac{60}{\pi n}\sqrt{\frac{2gH_{opt}}{\psi_{opt}}} \tag{3.10}$$

The outlet width was then estimated based on an empirical relation given as equation (3.11) [18].

$$\frac{b}{d_2} = 0.017 + 0.262\left(\frac{n_q}{n_{q,ref}}\right)^2 + 0.0093\left(\frac{n_q}{n_{q,ref}}\right)^3 \tag{3.11}$$

Unlike outlet width, inlet width cannot be established as a single parameter. Relevant parameters that determine the inlet width are the hub diameter and inner diameter. The diameter of the hub was taken to be 35 mm as per the industrial requirements. The inner diameter was estimated based on NPSH requirements. As discussed in section 2.2, the geometry at the inlet has a profound effect on cavitation characteristics, and hence, the inlet geometry is designed to minimize cavitation damage. An empirical relationship established for NPSH by Brekke that can be used to estimate the inlet diameter is shown as equation (3.12) [6].

$$NPSH = a\frac{c_{1m}^2}{2g} + b\frac{u_1^2}{2g} \tag{3.12}$$

Where a and b are empirical constants, and c_{1m} is the meridional component of fluid velocity at blade leading edge position. Equation (3.12) can be expressed in terms of the flow rate through the impeller and impeller inner diameter. With the flow rate taken as constant, the equation can be differentiated and then equated to zero to solve for the diameter that minimizes the required NPSH. Gulich [18] gives the corresponding relation for the required diameter as:

$$d_{inner} = \sqrt{d_h^2 + 10.6\left(\frac{Q_{imp}}{n}\right)^{\frac{2}{3}}\left(\frac{a+b}{b}\right)^{\frac{1}{3}}} \tag{3.13}$$

where a was taken to be 1.1, while b was taken as 0.95 [18]. In equation (3.13), Q_{imp} is not the same as Q_{opt}. Q_{opt} is the flow rate delivered from the pump at its operating point, while Q_{imp} is the flow rate through the impeller, which is greater than Q_{opt} by the amount of leakage. An estimate of Q_{imp} depends on an estimate of volumetric efficiency. The volumetric efficiency is determined based on an estimate of the overall efficiency, which is calculated according to an empirical relation given by[18] as:

$$\eta^{pump} = 1 - 0.095\left(\frac{Q_{ref}}{Q_{opt}}\right)^{0.20} - 0.3\left(0.35 - \log\frac{n_q}{23}\right)^2\left(\frac{Q_{ref}}{Q_{opt}}\right)^{0.05} \tag{3.14}$$

where Q_{ref} is taken as 1 m^3/s. Similarly, an estimate of the hydraulic efficiency can be made based on an empirical relation given as [18]:

$$\eta^h = 1 - 0.055\left(\frac{Q_{ref}}{Q_{opt}}\right)^{0.16} - 0.2\left(0.26 - \log\frac{n_q}{25}\right)^2\left(\frac{Q_{ref}}{Q_{opt}}\right)^{0.1} \tag{3.15}$$

Table 3.1: Design values defining the meridional section of the impeller

Design parameters	**Values**
Outer diameter, d_2	414 mm
Outlet width, b	17 mm
Hub diameter, d_h	35 mm
Inner diameter, d_1	98 mm
Shroud radius, r_s	16 mm
Axial length, I_a	26 mm

With an estimate of the hydraulic and overall efficiencies, the volumetric efficiency was determined by assuming the mechanical efficiency to be 100%. This implies that the power loss in bearings and disk friction is negligible compared to power supplied to the shaft. This is not an unrealistic assumption, since the mechanical efficiency for most large impellers is over 99.5% [18]. With the volumetric efficiency determined, the quantity Q_{imp} was estimated as being equal to Q_{opt}/η_v. With Q_{imp} established, the equation (3.13) was used to determine the inner diameter.

The inner and hub diameter provide the inner width, and the shroud radius was taken to be half the value of the inner width as per the recommendation from Karassik [22]. Shroud radius is part of the axial length shown in Figure 3.2, which was taken to be shroud radius plus 10 mm. The axial length does not have any meaningful impact on the hydraulic performance of the pump. It leads to the inlet of the impeller, which connects to inlet pipe. The inlet pipe was taken to be twice as long as the inner diameter to ensure uniform flow field at the impeller inlet. The numerical values defining the design of the meridional section are outlined in Table 3.1. This completes all the dimensions needed to design the meridional section of the impeller. The next design component of the impeller is blade.

3.2.1.2 Blade

Prior to designing the blade, it is important to establish the number of blades, Z, blade thickness, t, blade inlet angle, β_1, and blade outlet angle, β_2. There are some considerations when selecting the number of blades. If the number of blades is too large, the rotor-stator interaction becomes more intense and there is a greater risk of head curve instability [18]. On the other hand, if the number of blades selected is too low, the head output at design flow rate might be too low. A good range for most purposes is 5 to 7 blades [18]. As a starting point, the number of blades was selected to be 7.

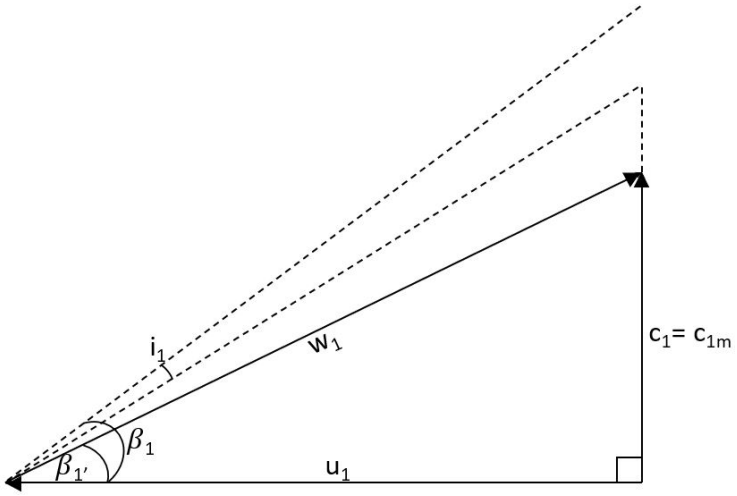

Figure 3.3: Velocity triangle at impeller inlet. c_1: Fluid absolute velocity, c_{1m}: Meridional component of fluid velocity, i_1: Blade incidence angle, u_1: Rotational velocity of impeller, w_1: Fluid relative velocity, $\beta_{1'}$:Angle of relative velocity vector to u_1, β_1: Blade inlet angle.

The blade thickness, t, is determined mainly in terms of the requirements for castability and material strength. An empirical rationale based on material strength provided by Gulich [18] yields a value of about 6 mm. The value for blade thickness has also been shown to impact the hydraulic performance of the pump. The numerical study done by Xu et al. [45] showed that the performance features of a plastic pump were worsen once the blade thickness exceeded 6 mm. The performance features of the pump for blade thickness less than 6 mm were more or less the same as those of the pump with blade thickness of 6 mm. Hence, the blade thickness was chosen to be 6 mm.

The blade inlet and outlet angles are established based on the velocity triangle. These angles determine the curvature and total length of the blade. The velocity triangle at the impeller inlet is shown in Figure 3.3.

In Figure 3.3, the velocity u_1 is calculated using the radius at the leading edge position in the meridional plane and the impeller rotational speed. The meridional component of fluid velocity, c_m1, is determined using the flow rate through the impeller and area defined by the contours of hub and shroud at leading edge position. Also, it is important to note that the fluid is assumed to exhibit no pre-rotation, *i.e.* the fluid velocity has no component in the circumferential direction as it approaches the impeller, which is true in most cases [18]. Hence, the fluid's absolute velocity is in the meridional direction, *i.e.* $c_1 = c_{1m}$.

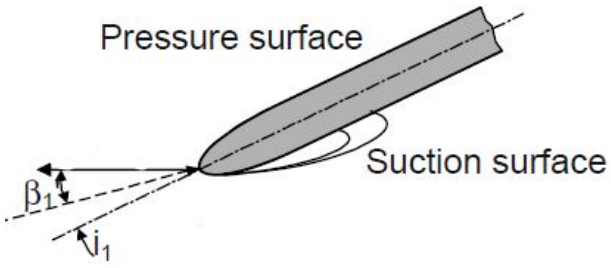

Figure 3.4: Blade incidence causing flow separation at blade leading edge (source: [18]).

Another important point to note in Figure 3.3 is that the blade inlet angle is not the same as the angle of the relative velocity vector. This discrepancy exists because the relative flow angle, $\beta_{1'}$, does not account for blade incidence and blade blockage effects.

Blade incidence, i_1, is the angle between blade camber line and fluid relative velocity vector. It results in excess local velocities around the leading edge and may even result in flow separation if the incidence angle is made too large. This phenomenon is illustrated in Figure 3.4, where the blade incidence causes flow separation. For this reason, the incidence angle was chosen to be 2°. Lower incidence angle also means reduced cavity length around the blade leading edge.

Another key factor is the blade blockage effect, which accounts for the increase in the meridional component of the fluid velocity immediately downstream of the blade leading edge. This happens because of the finite thickness of the blade; *i.e.* the flow area decreases immediately downstream of the leading edge, and hence the meridional component of the flow velocity increases. The blade blockage effect is quantified using the blade blockage ratio at inlet, ζ_{in}, defined as equation (3.16) [21].

$$\zeta_{in} = \frac{tZ}{2\pi R_1 sin\beta_1} \tag{3.16}$$

where R_1 is the radius of shroud at blade leading edge position. Equation (3.16) is essentially the ratio of the length occupied by blade thickness at the shroud to the diameter of the shroud at leading edge position.

Taking into account both of these effects, the blade inlet angle can be calculated using

Figure 3.3 as:

$$\begin{aligned} \beta_1 &= \arctan \frac{(1-\zeta_{in})^{-1} c_{1m}}{u_1} + i_1 \Rightarrow \\ \beta_1 &= \arctan \frac{\left(1 - \left(\frac{tZ}{2\pi R_1 \sin \beta_1}\right)\right)^{-1} c_{1m}}{u_1} + i_1 \end{aligned} \tag{3.17}$$

where the meridional component of fluid velocity has been amplified using the blade blockage ratio. As shown in equation (3.17), the blade inlet angle is expressed implicitly, since it is part of the blade blockage ratio on the right-hand side of the equation. Therefore, it was determined iteratively with convergence obtained at the value of 33°.

Unlike blade inlet angle, the flow field inside the impeller channel has to be taken into account for the blade outlet angle. An important flow phenomenon inside the blade channel that influences the flow condition at impeller outlet is known as slip phenomenon, which is illustrated in Figure 3.5. It refers to the deviation of flow streamlines towards the blade pressure side at the impeller outlet, which results in dissipation losses. These may be reduced by increasing the number of blades, but, as mentioned earlier, this may result in head-curve instability. As shown in Figure 3.5, there is significant deviation of the flow streamlines from the dashed lines towards the impeller outlet, where the dashed lines represent the blade-congruent flow.

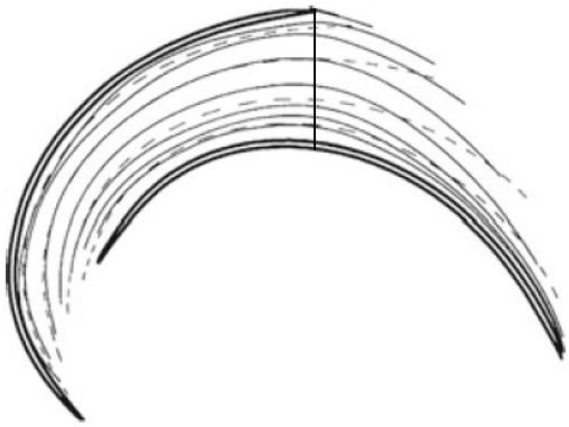

Figure 3.5: Illustration of slip phenomenon with flow streamlines deviating towards the blade pressure side beyond the solid vertical line [18].

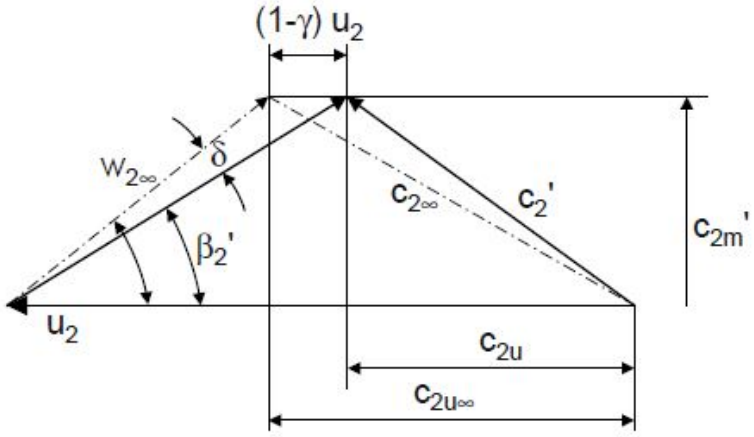

Figure 3.6: Velocity triangle at impeller outlet. The dashed lines represent the blade-congruent flow, while the actual flow is represented by the solid lines. The superscript ' represents the flow quantities with blade blockage effects taken into account. γ: Slip factor, δ: Deviation angle. [18]

This phenomenon means that the angle of the relative velocity vector of the flow decreases toward the impeller outlet, which is illustrated in Figure 3.6. In Figure 3.6, the term γ is known as the slip factor, which quantifies the slip phenomenon. It can have values between 0 and 1. The greater its value, the smaller will be the deviation of the streamlines towards the outlet. A gamma value of one implies blade-congruent flow and hence no deviation. A comprehensive review of slip factors for centrifugal impellers is provided in [8]. In theory, it is possible to have zero deviation of the streamlines with an infinite number of blades. Deviation is also quantified by the angle δ, which is the difference between the blade outlet angle and the angle of the relative velocity vector at the outlet. Also, it is important to note here that, unlike the velocity triangle at inlet, the tangential component of the absolute fluid velocity is not zero. This would be an unreasonable assumption, since that would imply that the theoretical head that can be generated, according to equation (3.4), is zero, or negative. The difference between the tangential component of velocity for actual flow, c_{2u}, and that for the blade-congruent flow, $c_{2u\infty}$, according to Figure 3.6, can be expressed as:

$$c_{2u\infty} - c_{2u} = (1 - \gamma)u_2 \tag{3.18}$$

The equation (3.18) can be manipulated and solved for the term c_{2u} as a function of

the blade outlet angle, which is shown as equation (3.19) [18].

$$c_{2u} = u_2 \left(\gamma - \frac{c_{2m} \left(1 - \zeta_{out}\right)^{-1}}{u_2 tan\beta_2} \right) \tag{3.19}$$

where the meridional component of the velocity at the outlet has been amplified using the blade blockage ratio in the same way as is done for the case of meridional velocity at the inlet. For the slip factor, Weisner [43] published an empirical relation for the slip factor prediction, which can be expressed as equation (3.20) for radial impellers that are used in centrifugal pumps [18].

$$\gamma = 0.98 \left(1 - \frac{\sqrt{sin\beta_2}}{Z^{0.7}} \right) \tag{3.20}$$

Equation (3.20) can be substituted in equation (3.19), which gives another expression for c_{2u}. This expression can then be substituted in equation (3.4) to solve for the theoretical head in terms of the blade outlet angle. The resulting equation is given as:

$$H_{th} = \frac{u_2^2}{g} \left(0.98 \left(1 - \frac{\sqrt{sin\beta_2}}{Z^{0.7}} \right) - \frac{c_{2m} \left(1 - \zeta_{out}\right)^{-1}}{u_2 tan\beta_2} \right) \tag{3.21}$$

The theoretical head can be converted to the actual head using hydraulic efficiency. Multiplying the equation (3.21) by the hydraulic efficiency and expanding the terms c_{2m} and ζ_{out} gives:

$$\begin{aligned} H &= \frac{\eta^h u_2^2}{g} \left(0.98 \left(1 - \frac{\sqrt{\sin \beta_2}}{Z^{0.7}} \right) - \left(\frac{Q_{imp}}{\pi b d_2} \right) \frac{\left(1 - \zeta_{out}\right)^{-1}}{u_2 \tan \beta_2} \right) \Rightarrow \\ H &= \frac{\eta^h u_2^2}{g} \left(0.98 \left(1 - \frac{\sqrt{\sin \beta_2}}{Z^{0.7}} \right) - \left(\frac{Q_{imp}}{\pi b d_2} \right) \frac{\left(1 - \frac{zt}{\pi d_2 sin\beta_2}\right)^{-1}}{u_2 tan\beta_2} \right) \end{aligned} \tag{3.22}$$

Given the desired head output at the design flow rate and the estimate of hydraulic efficiency established in section 3.2.1.1, equation (3.22) was used to iteratively solve for the outlet angle with all the other variables known. The convergence was obtained at a value of 29°.

It is important to note that equation (3.22) could have involved more terms had there been a circumferential component of the fluid velocity at the impeller inlet. As discussed

Table 3.2: Design values defining the blade of the impeller

Design Parameters	**Values**
Number of blades, Z	7
Blade width, t	6 mm
Blade inlet angle, β_1	33°
Blade outlet angle, β_2	29°

earlier, the fluid inflow is assumed to exhibit no pre-rotation, hence having no circumferential component when it approaches the blade leading edge. This implies the term c_{1u} in equation (3.4) is zero. However, it should also be noted that the additional terms would have made a negative contribution towards the head delivered. This is why it is important to ensure that fluid approaches the impeller inlet with no pre-rotation. Equation (3.22) is important not only for establishing the blade outlet angle, but also helps explain that the head delivered by the impeller depends on a number of factors, such as hydraulic efficiency, impeller rotational velocity at the outlet, and outlet width. Also, it shows that different sets of values for variables on the right hand side of the equation can yield the same value of head. However, each set of values might yield different efficiency for the pump from the other. For example, according to equation (3.22), increasing the outer diameter of the impeller and decreasing the outlet width by the same factor will yield the same head output, but this comes at the cost of increased disk friction losses. Selecting a particular set of values for parameters that achieves the desired head output and maximizes the efficiency is where optimization algorithms become important. However, for design optimization, a baseline design is needed. The empirical relations and theory used for the design, including the blade outlet angle, are reliable ways to obtain a baseline design.

The values established defining the design of the blade are outlined in Table 3.2. However, these values do not define the procedure of delineating the blade profile. Here the circular arc method was used [34]. The method is illustrated in Figure 3.7. The inner circle defines the position of the leading edge of the blade, while the outer circle defines the position of the trailing edge. At a point, A, on the outer circle, a line is drawn with an angle equal to that for the blade outlet, β_2, to the tangent. Thereafter, a normal to this line is drawn (line AM in Figure 3.7). From the center, O, another line of length equal to the radius of the inner circle is then drawn rotated in the same direction as the rotation of the impeller by the angle $\beta_1 + \beta_2$, which intersects the inner circle at point B. The line joining point A and point B intersects the inner circle again at point E. The normal to the line AE from its midpoint intersects another normal drawn from point A at point M, which represents the center of the arc. Points A and E, together with the center point, M,

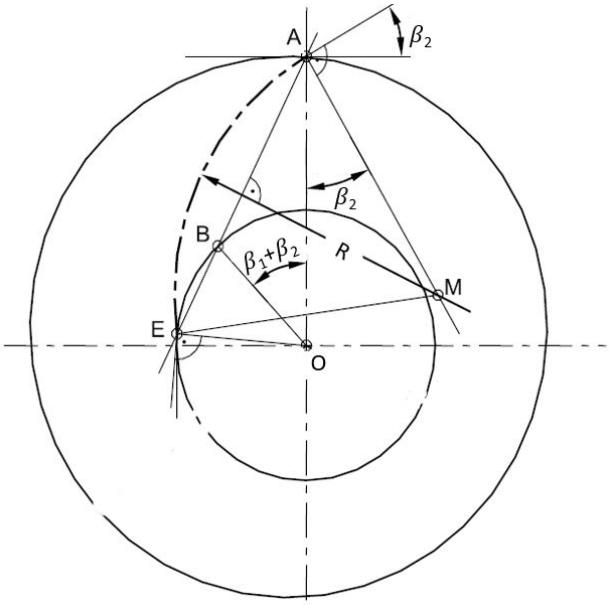

Figure 3.7: Circular arc method for the design of blade. β_1: Blade inlet Angle, β_2: Blade outlet angle, A: Point of trailing edge, B: Construction point for line AE, E: Point of leading edge, M: Center of the arc, R: Radius of the arc. (source: [34])

can then be used to create the arc that represents the camber line of the blade.

The camber line represents a symmetry line for the blade profile, about which the blade pressure and suction profiles are delineated. For its better cavitation performance discussed in section 2.2, an elliptic arc with a minor radius of 3 mm, and major radius of 6 mm was used to profile the leading edge. This merged nicely with the chosen value of 6 mm for blade thickness. The trailing edge was made blunt, but was trimmed by 2 mm to reduce the intensity of rotor-stator interactions, *i.e.* the radius of the outer circle shown in Figure 3.7 is 2 mm shorter than that of the meridional section ($d_2/2$ in Figure 3.2). This completes the design of the impeller. The next design component is the volute.

3.2.2 Volute Design

The volute was designed using the constant velocity method discussed in section 2.2. Volutes designed with this method have cross-sectional areas that change in proportion to the angular displacement of the tongue, which is illustrated in Figure 1.3. This method involves design constants that are functions of the specific speed [38]. These design con-

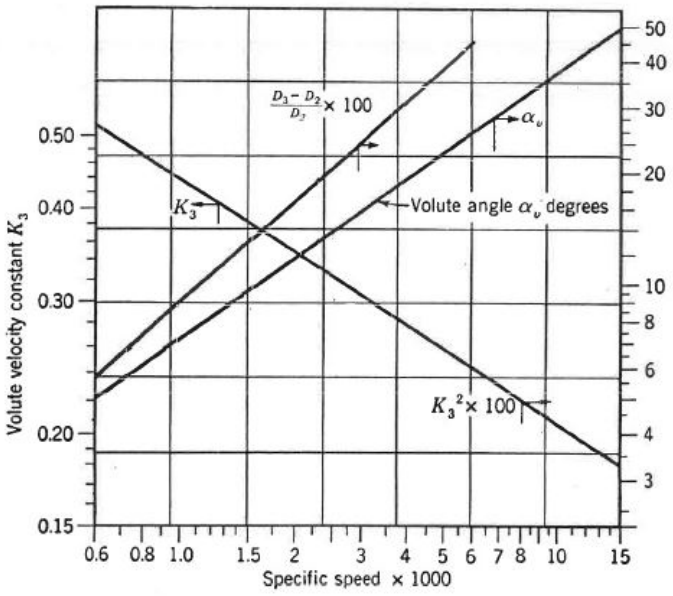

Figure 3.8: Empirical design constants for the volute (source: [38])

stants define the geometrical shape of the volute, such as the gap width and throat area. For this method, the specific speed is calculated using a different set of units than those used to calculate the specific speed value of the impeller design. In equation (3.7), while n is still used as the number of revolutions per minute, Q_{opt} has the units of gallons per minute, and H has the units of feet.

Having determined the specific speed, a speed constant, K_3 can be determined using Figure 3.8 that is used to calculate the average velocity in the volute. It is important to note that the specific speed value used for design is outside the range of the graph and, hence, extrapolation was used to establish the design constant. Once the constant, K_3, has been established, the average velocity in the volute, c_3 can be determined using the equation:

$$c_3 = K_3\sqrt{2gH_{opt}} \tag{3.23}$$

The average velocity can then be used to determine the throat area, A_v, which is the cross-sectional area of the volute throat shown in Figure 1.3. The volute throat is designed to deliver the flow rate at deign point, Q_{opt}, which can be used together with the known average velocity in the volute to establish the required volute throat area. The value for

volute throat area doesn't include the gap width, $D_3 - D_2/2$, shown in Figure 1.3. The gap width is a separate entity that is important to reduce the noise of pressure pulsations.

The gap width can also be established from Figure 3.8, where the relevant term is expressed as a fraction of the impeller outer diameter, D_2, which has been established in previous section. Again, extrapolation was used and the value for gap width was obtained as 18 mm. This implies the radial distance between the impeller and the tongue is 18 mm. Another relevant parameter for volute design that specifies the position of tongue is the volute angle, α_v, shown in Figure 3.8.

However, for the case of low specific-speed pumps, the position of the tongue does not have a significant impact on the performance features [38]. Ideally, the position of the tongue must match the angle of the absolute velocity of fluid leaving the impeller so that there are no shock or separation losses. In this case, the angular displacement of the position of the tongue from the vertical axis in the clockwise direction in Figure 1.3 was chosen as 12.5°. This completes the list of design parameters needed for volute, and hence, for the pump. These design parameters were used to draft a CAD model, which was then used to simulate the flow through the pump. The details of the numerical framework used for the simulations are described in the subsequent section.

3.3 Numerical Model

The numerical simulations were carried out in TCAE, which is a commercial simulation package built on Openfoam [37]. The simulations involved the solution of the steady-state, incompressible Reynolds-Averaged Navier-Stokes (RANS) equations using the Shear Stress Transport (SST) $k-\omega$ model developed by Menter [27]. The steady-state RANS equations are given as:

$$\begin{aligned} \nabla \cdot \boldsymbol{u} &= 0 \\ \boldsymbol{u} \cdot (\nabla \boldsymbol{u}) &= v_{eff} \nabla^2 \boldsymbol{u} - \nabla p_k + \boldsymbol{g} \end{aligned} \tag{3.24}$$

where $\boldsymbol{u}$ is the velocity vector, v_{eff} is the effective kinematic viscosity, and p_k is the kinematic pressure $p_k = p/\rho$. The effective kinematic viscosity is defined as the sum of the kinematic viscosity, v, and turbulent kinematic viscosity, v_t. The turbulent kinematic viscosity is modelled using the chosen turbulence model, which is SST $k-\omega$ for this study.

The SST $k-\omega$ model is a combination of standard $k-\omega$ and $k-\epsilon$ models. The standard $k-\omega$, developed by Wilcox [44], is undesirable for its strong sensitivity to the free stream conditions [28]. Menter [27] developed SST $k-\omega$ model to solve this problem

that is a mixture of standard $k-\omega$ and $k-\epsilon$ models, *i.e.* it transforms to $k-\omega$ model near the surface and to $k-\epsilon$ model in free stream conditions. This is done by means of a blending function that is dependent on the distance from the wall. Further details on the turbulence models and the blending function can be found in Appendix B.

The solver is based on Finite Volume Method (FVM), spatially discretized to first-order for better convergence, which reduces the governing differential equations to a system of linear equations to be solved for each cell. The pressure-velocity coupling required for the solution to the system is done using the SIMPLEC algorithm. Further details about the algorithm and pressure-velocity coupling can be found in [40]. The stability of the solution for each flow rate was ensured with the residuals converging to 10^{-4}, or less for all the flow variables over the last 100 iterations, or so. However, no convergence criteria were used, which can often be misleading, since it takes only the last two iterations into account to determine convergence. The iterations of the numerical solutions are performed on the mesh.

The mesh was obtained using the `snappyHexMesh` utility of OpenFoam [19]. It works by first obtaining a base mesh with hexahedral cells and then refining the base mesh locally near the geometrical features based on the refinement levels specified. The degree of refinement needed depends on the geometrical complexity, so increased refinement levels were specified for features such as blade leading edge, and volute tongue. This results in a castellated mesh that is snapped onto the surface. The result is a smooth mesh that preserves the surface features. The mesh was obtained for three different geometries: Inlet pipe, Impeller, and Volute. The pump geometry were created in FreeCAD [14]. A fully parametric model for pump based on design variables was developed in Python using FreeCAD module, which is shown in Appendix A. The geometry was imported into TCAE for meshing. The meshes were connected through interfaces.

The interface between the rotor and stator was set as an Arbitrary Mesh Interface (AMI), also known as Frozen Rotor. AMI maps the variable directly across the interface. Another method, known as the Mixing Plane Interface (MPI), first computes the average value of the variable and then maps the average value across the interface.

The medium selected was Water at Standard Temperature and Pressure (STP). Volumetric flow rate of the medium was chosen as the boundary condition for outlet. For inlet, the total pressure of 1 atmosphere (atm) was specified as the boundary condition. All the walls were treated with no-slip boundary condition with standard wall functions. The boundary layer effects were captured by adding 5 layers in the mesh near the wall region.

Chapter 4

Results and Analysis

This chapter focuses on the results of the numerical simulations that were performed. The grid independency results are outlined, followed by the performance features of the baseline design. The results of the baseline design are used as a basis for changing the design parameters and then evaluating the impact in terms of the change observed in the performance characteristics.

4.1 Grid Independency Results

The grid independence study was done using four different meshes, where the number of mesh elements were successively increased. The change was made in terms of the background mesh size only; *i.e.* the refinement levels were kept the same to systematically and uniformly vary the mesh size throughout the domain. The meshing feature described in section 3.3 works by allowing the user to specify the minimum and maximum levels of refinement and another level used for gap refinement for each component. The minimum level was specified as zero, while the maximum level was specified as two for all components. The exception were the components with simplified geometry, such as the outlet and inlet of the pump, where the maximum level of refinement was specified as one. The gap refinement level was specified as three. The resulting mesh was deemed satisfactory for all the background mesh sizes upon visual inspection. The coarsest mesh had mesh size of 3.2 mm, and the mesh size was successively reduced by 0.2 mm. The results of the mesh independence study are shown in Figure 4.1. The key performance parameters, such as head and efficiency, of the Baseline design, *i.e* the design obtained using the methodology

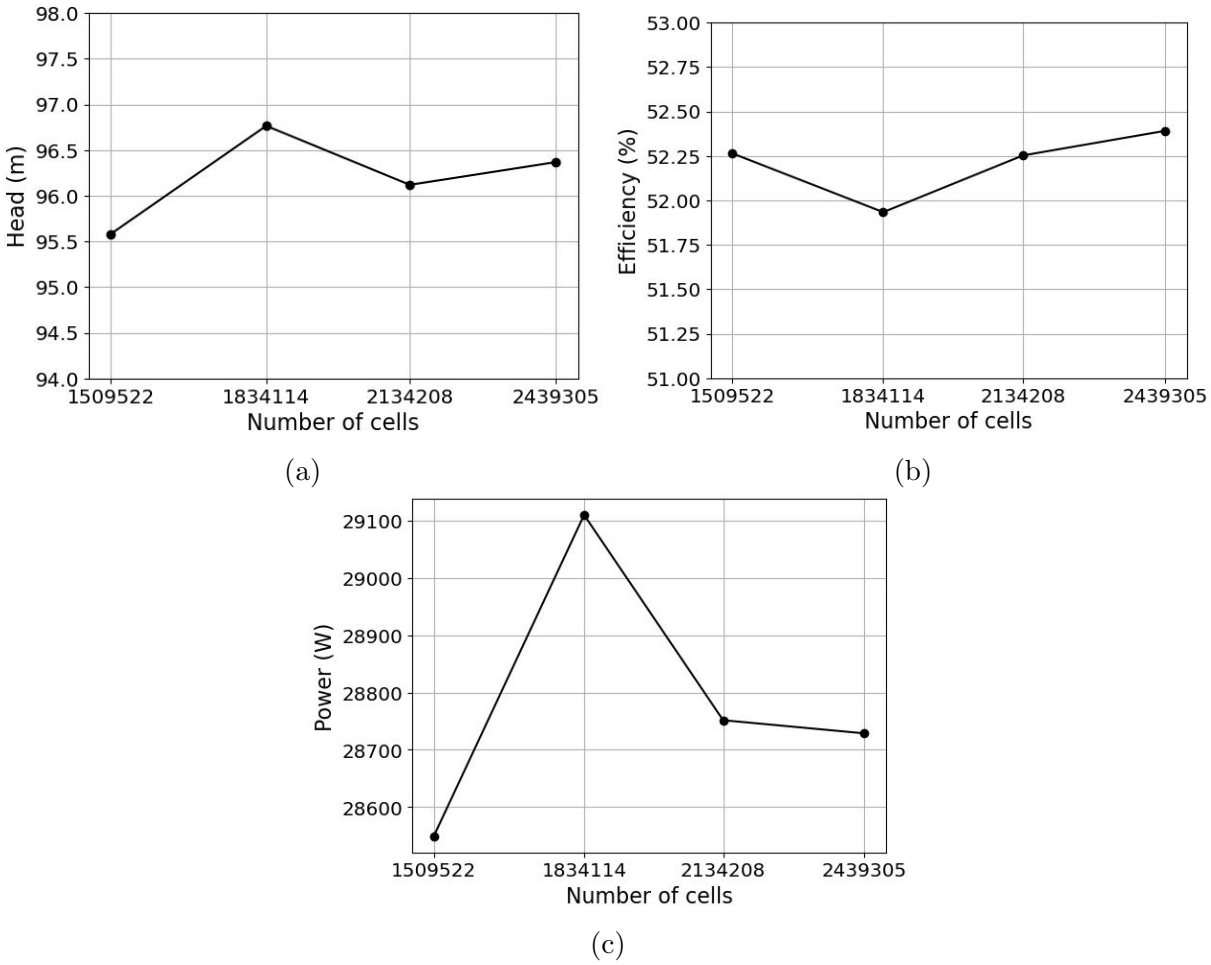

Figure 4.1: Grid convergence study at the design flow rate

outlined in chapter 3, were assessed at the design flow rate of 253 USGPM, to evaluate the grid independence of the simulation.

As can be inferred from Figure 4.1, performance characteristics do not change significantly as the mesh size is reduced. As the mesh size is reduced from the 3.2 mm (1, 509, 522 cells) to 3.0 mm (1, 834, 114 cells), the percentage changes are 1.24, 0.63, and 1.97 for head, efficiency and power, respectively. Further refinement from the mesh size of 3.0 mm to 2.8 mm (2, 134, 208 cells) yields the percentage changes of 0.67, 0.61, and 1.23 for the same quantities. Even further refinement of the mesh size of 2.8 mm to 2.6 mm (2, 439, 305 cells) results in the head output being changed by 0.26%, efficiency being changed

by 0.26%, and power by 0.08%. Although not included in this case, a good practise is to conduct simulations at a much coarser grid as well (with number of cells in the order of 10^5 or so). The grid convergence study was also done at under- (150 USGPM) and overload (350 USGPM) conditions; the same pattern was observed where the performance characteristics changed by less than 1% as the grid was refined from 2.8 mm to 2.6 mm. Hence, the mesh size of 2.8 mm with 2,134,208 cells was used for all simulations. The resulting meshes obtained for the impeller and volute for the mesh size of 2.8 mm are shown in Appendix C. The Figures C.1 and C.2 show the mesh refinement and boundary layers near the impeller inlet (blade leading edge) and impeller outlet (blade trailing edge), respectively. Figure C.4 shows the mesh refinement near the tongue region of the volute.

4.2 Performance Features of Baseline Design

Performance characteristics are evaluated in terms of head output, efficiency, and power required as a function of the flow rate through the pump. The pump characteristics are shown in Figure 4.2.

As shown in Figure 4.2, the head curve almost continuously decreases as the flow rate increases. There is slight instability observed near the shut-off point, *i.e.* the slope of head-capacity curve is positive at the flow rate close of zero. Additionally, the curve steepness near the design point is close to zero, which is not desirable. This implies that the head change is negligible as the flow rate varies around the design point. Another undesirable characteristic can be observed in the plot for efficiency, where the BEP is located at more than twice the value of the design flow rate. This is typical of the low specific speed pumps and has been noted in other studies as well. For example, Choi et al. [11] noted and showed that BEP is located at a much higher discharge than the design flow rate for the case of low-specific speed pumps. A possible remedy is the reduction of the volute throat area, which was attempted for the first design iteration. This has been shown to increase the steepness of the head-capacity curve and shift the BEP closer to the design point [9]. An attempt has been made to explain why this is the case.

4.3 First Design Iteration

For the first design iteration, the volute throat area was reduced by 50%. It is possible to get an even steeper head-capacity curve if the throat area is further reduced. However, as will be shown, reduction in throat area leads to significant viscous losses under overload

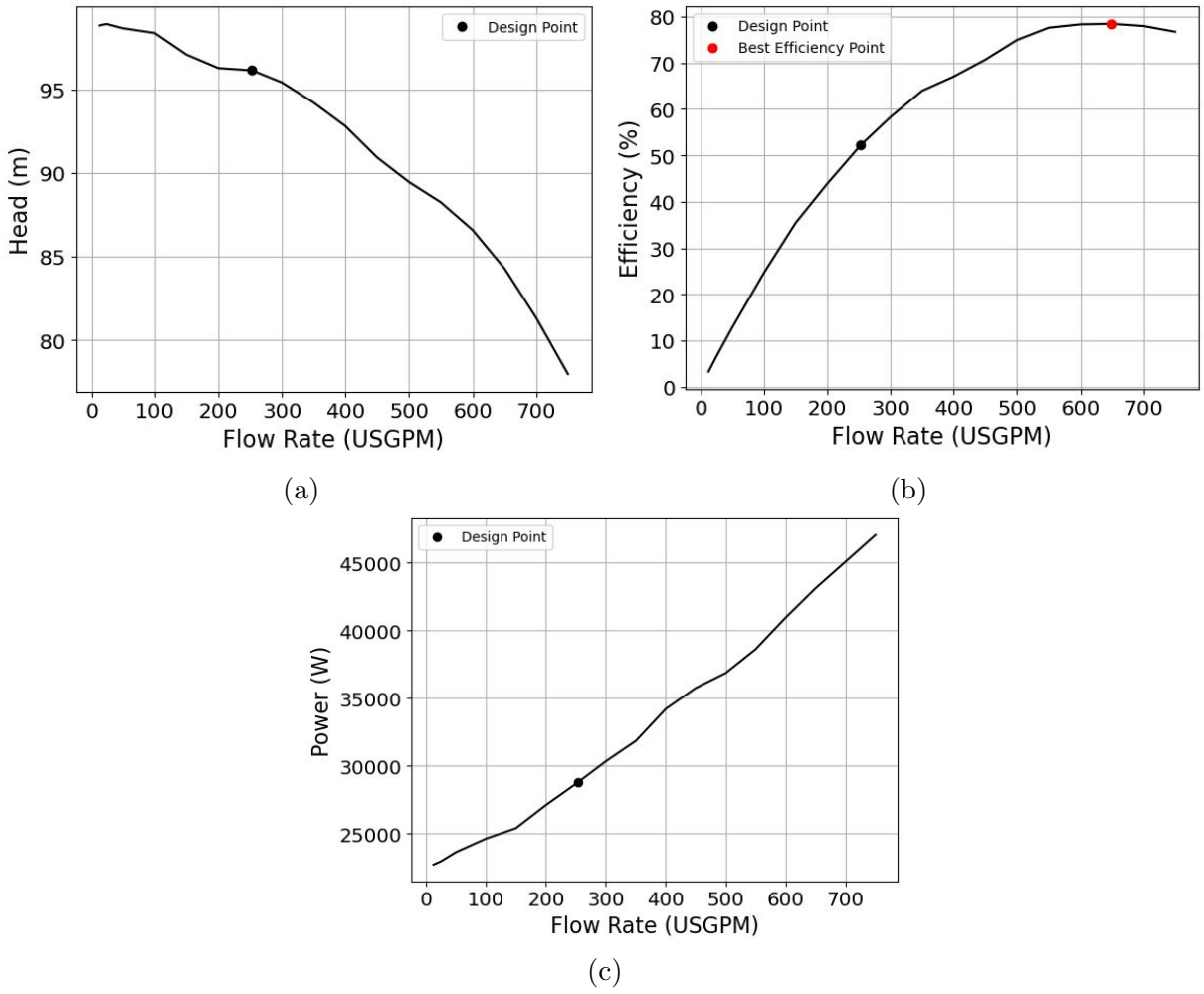

Figure 4.2: Performance characteristics of the baseline design

conditions, which reduces the delivered head. Reducing the throat area even further will make these effects more pronounced, which may even be observed at the design point. Therefore, the throat area was not further reduced. The reduction by 50% in throat area lead to significant improvements in performance characteristics as shown in Figure 4.3. Figure 4.3 shows that the head-capacity curve is much steeper compared to that for the baseline design, although the head output at the design point is almost the same for both cases. Additionally, the BEP for the improved design is much closer to the design flow rate than what is observed for the case of the baseline design. Another favorable outcome is the reduction in power requirements for discharge to 500 USGPM. It helps to analyze the

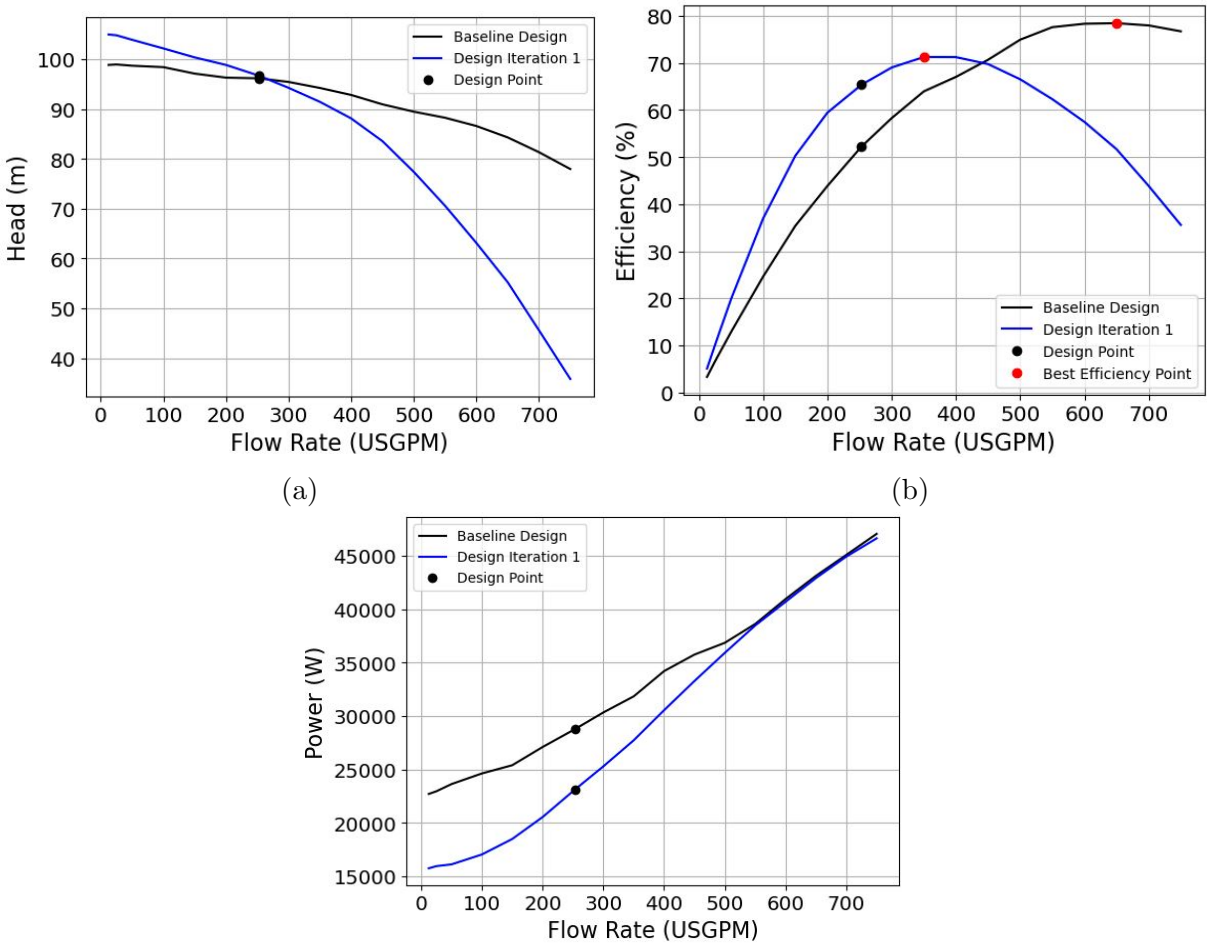

Figure 4.3: Performance characteristics resulting from reduction in volute throat area of the baseline design in comparison to those of the baseline design

internal flow fields of the pump to better understand these effects.

4.3.1 Effect of Throat Area Reduction on the Internal Flow Field

Figure 4.3b shows that the efficiency of the first design iteration is greater than that of the baseline design up to the discharge of around 450 USGPM. An important reason for this improvement is shown in Figure 4.3c, which shows that there is a significant difference in

the power requirements for the two design options, with the baseline design consuming a lot more power. This difference closes in as the flow rate approaches around 500 USGPM. The reduced power requirement means an increase in overall efficiency as per equation (3.3).

Power is a measure of the energy supplied to the shaft to rotate the impeller. This energy supplied is proportional to the pressure difference between the blade pressure and the suction sides. The greater the pressure difference, the greater the amount of energy required to rotate the blades. This implies that the pressure difference between the blade pressure and suction sides for the baseline design is greater than that for the first iteration design. Therefore, the baseline design requires more power, especially at underload and design conditions. This is illustrated in Figure 4.16, which shows the pressure distribution over a blade in the streamwise direction at multiple flow rates. It is clear from the figure that the baseline design experiences a greater difference in pressure between the pressure and suction sides of the blade than that observed for the first iteration design. It is important to note that these plots represent the pressure distribution at the midspan of the blade height for a particular blade in both designs. Figure 4.4 shows the pressure distribution over the blade height for the same blade in both designs at 80% of its length in the streamwise direction at 100 USGPM. This gives an idea of pressure variation over a blade in direction normal to streamwise direction. Once again, the pressure difference is much greater for baseline case than for the first iteration design. The deviation, however, is minimal at the flow rate of 600 USGPM, which is consistent with what is shown in Figure 4.3c, where the power requirements for both designs at this discharge rate are almost the same. These results can be used to conclude that the flow field is more uniform in the first iteration design than that in the baseline case, leading to an increase in efficiency. However, this effect is counteracted by the reduced head output of the first iteration design past the design point, which contributes to the decrease in overall efficiency.

Reduced head output at higher flow rates is primarily a result of the dramatic pressure drop towards the outlet for the first design iteration. With excess flow velocities and reduced cross-sectional area of the volute, the rotor-stator interaction intensifies. This is further illustrated in Figure 4.5, which shows the total pressure, p^T, distribution (representative of mechanical energy) for both designs at flow rates of 400 USGPM and 600 USGPM. Compared to the baseline case, the first iteration design experiences significantly more viscous losses at higher flow rates near the tongue region, leading to dramatic pressure drop towards the outlet. The effect may not seem significant at the flow rate of 400 USGPM but becomes much more consequential at the higher flow rate of 600 USGPM. The Turbulent Kinetic Energy (TKE) at the same flow rate also gets more amplified near the tongue region compared to that observed for the baseline case. This is further illustrated in

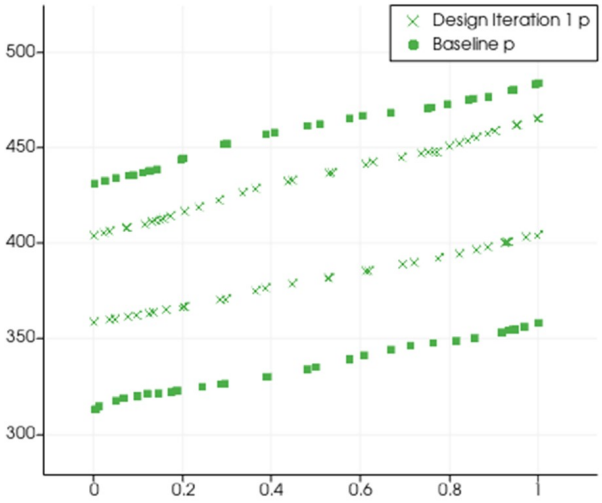

Figure 4.4: Pressure distribution in Pascals over the blade height at 100 USGPM. Point 0 corresponds to the shroud and point 1 corresponds to the hub of the impeller.

Figure 4.6 which shows the TKE distribution in the pump at 600 USGPM for both cases. Similar results were obtained in [9], where a region of high TKE was observed downstream of the tongue under overload conditions as the volute throat area was reduced. This signifies that mixing and dissipation losses near the volute tongue become more pronounced under overload conditions as the volute throat area is reduced. Figure 4.7 can be used to reach the same conclusion, which shows the head delivered from the impeller and the head loss incurred from impeller outlet towards volute outlet for each design. While there isn't any significant difference in head delivered by the impeller between the two cases at all flow rates, the head loss in volute gets significantly pronounced as the flow rate increases. Hence, the overall effect of volute throat reduction is the decrease of the head delivered and the overall efficiency at higher flow rates.

It is expected that the dramatic pressure drop under overload conditions will lead to a marked increase in cavitation. However, as shown in Figure 4.8a, the NPSH values for both designs are almost the same at all discharge rates. This is because NPSH accounts for cavitation occurring at the inlet of the pump and both designs experience similar cavitation behaviour in the inlet region. As shown in Figure 4.5, the dramatic pressure drop occurs near the tongue region, which is not captured by NPSH. The true measure of cavitation is provided in Figure 4.8b, which shows the volume of the domain expressed as percentage of the total volume where cavitation occurs. Figure 4.8b shows that there is a marked increase in the cavitating volume for the first iteration design once the discharge rate exceeds 500

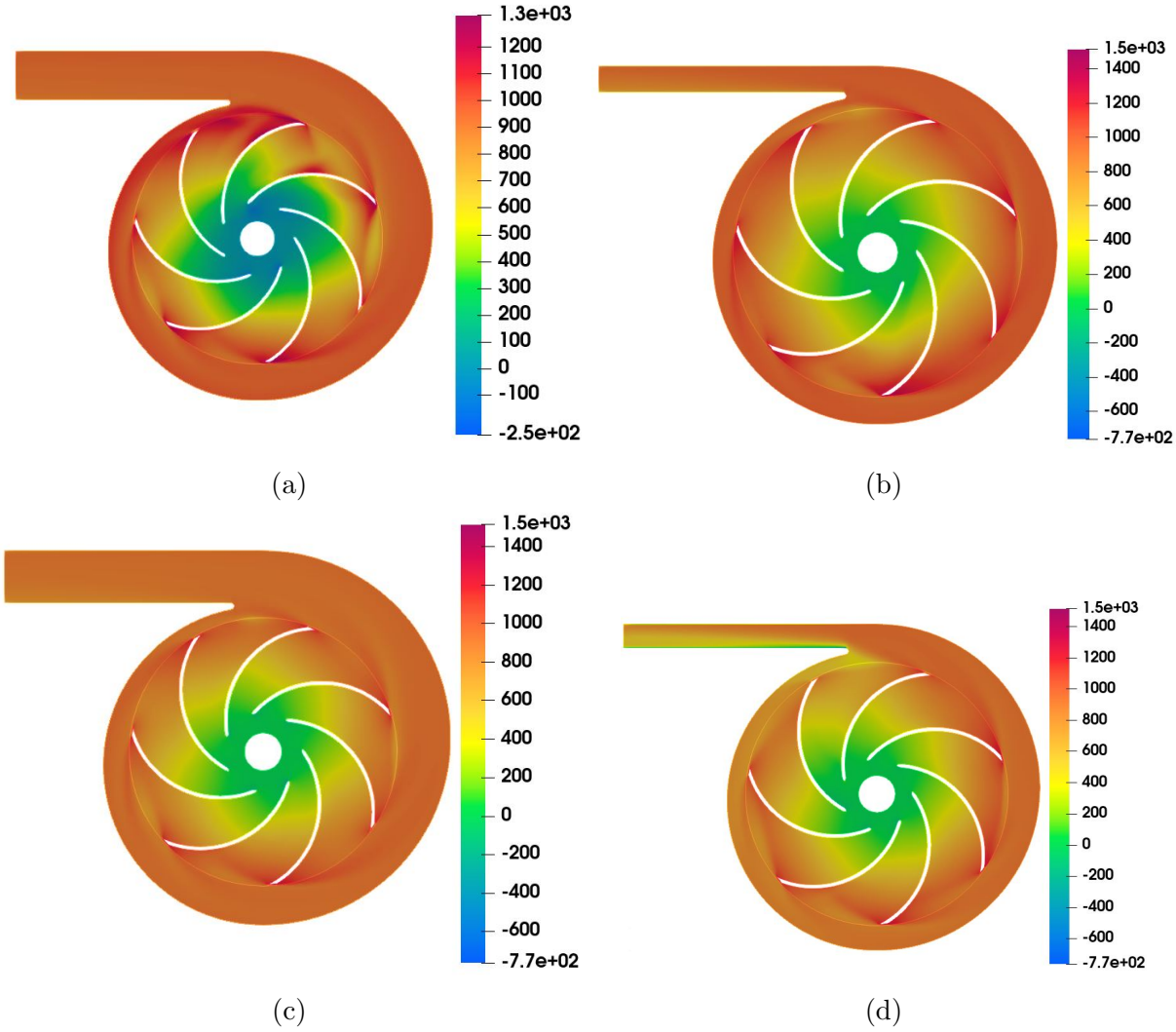

Figure 4.5: Distribution of total pressure (mechanical energy) in the pump for (a) Baseline at 400 USGPM, (b) First iteration design at 400 USGPM, (c) Baseline at 600 USGPM, and (d) First iteration design 600 USGPM.

USGPM. This is in line with what is shown in Figure 4.5d. Although there is a significant head drop at the discharge rate of 400 USGPM, as shown in Figure 4.5b, it does not cause excessive cavitation. The cavitation performance of both designs is similar up to a discharge rate of 500 USGPM.

Significant viscous losses at higher flow rates manifest themselves in the form of a

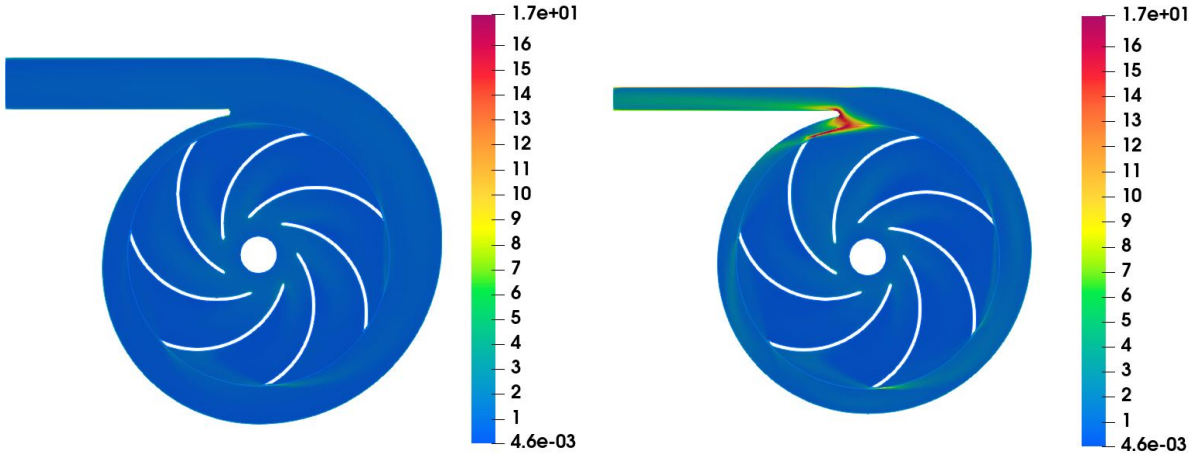

(a) (b)

Figure 4.6: Distribution of Turbulent Kinetic Energy (TKE) at the flow rate of 600 USGPM for (a) Baseline design and (b) First iteration design.

steep decline in the head delivered, which reduces overall efficiency. This is why the head-capacity curve of the first iteration design is much steeper than that for the baseline case. At discharge rates lower than 500 USGPM, the uniformity of the flow field in the first iteration design leads to the reduced power requirements which, in turn, increases the overall efficiency. The net result is an increase in efficiency at the design point and the shift of BEP from higher to lower discharge rate for the first iteration design. The performance features can be improved even further by reducing the gap width, which was attempted for the second design iteration.

4.4 Second Design Iteration

For the second design iteration, the volute gap width was reduced by 50%. It is possible to reduce the gap width even further, which may lead to even better hydraulic performance. However, with the gap width reduced by 50%, the radial distance between impeller outlet and tongue is 9 mm. Even further reduction would significantly increase the rotor-stator interactions in this region and lead to increased radial force on the impeller. This, in turn, will result in undue forces being experienced by the shaft. Hence, the gap width was not reduced any further. The reduction of the gap width by 50% leads to some improvement in performance characteristics as shown in Figure 4.9. The improvement for

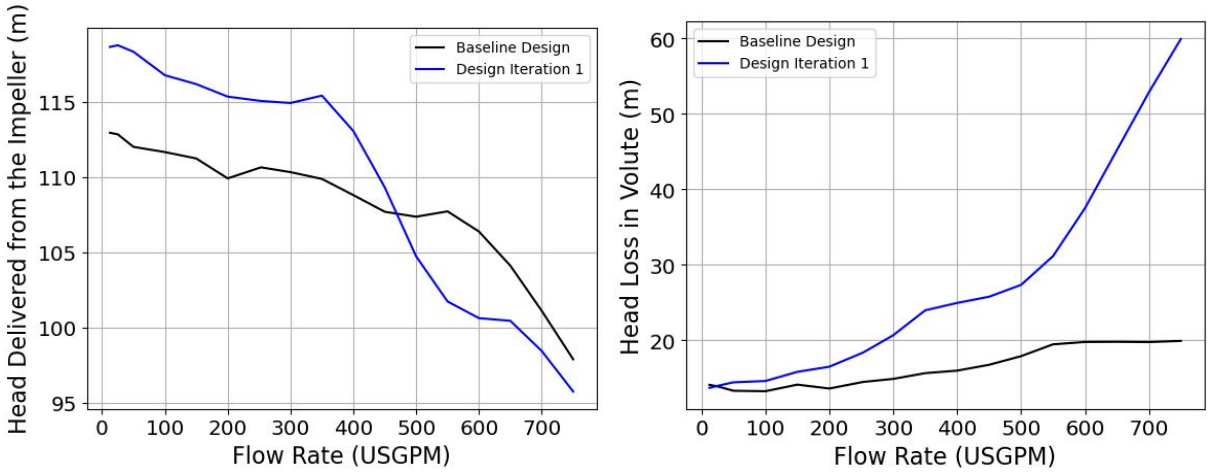

(a) (b)

Figure 4.7: (a) Head delivered from the impeller and (b) Head loss in volute for the two designs

the second iteration relative to the first iteration is not as pronounced as was observed for the case of the first iteration relative to the baseline case. The power requirements for the two cases are almost the same. The head-capacity curve shows a vertical shift for the second iteration design relative to the first iteration design, and the efficiency of the second iteration design has also improved slightly for flow rates exceeding 200 USGPM. The performance features at the design point for the three designs discussed so far are outlined in Table 4.1. As mentioned above, the head delivered for the first design iteration is not significantly different from that delivered from the baseline design at the design point. However, there is a significant change for the head delivered from the second iteration design compared to that delivered from the baseline design. The efficiency at the design point for the second iteration design has also improved compared to that of the first iteration design at the design point. However, the relative change in power requirements is not significant. Once again, internal flow fields were investigated to better understand the impact of the reduction of gap width.

4.4.1 Effect of Gap Width Reduction on the Internal Flow Field

The improvement in performance is simply a result of greater head output generated at the impeller in the second iteration design relative to that for the first iteration design, while

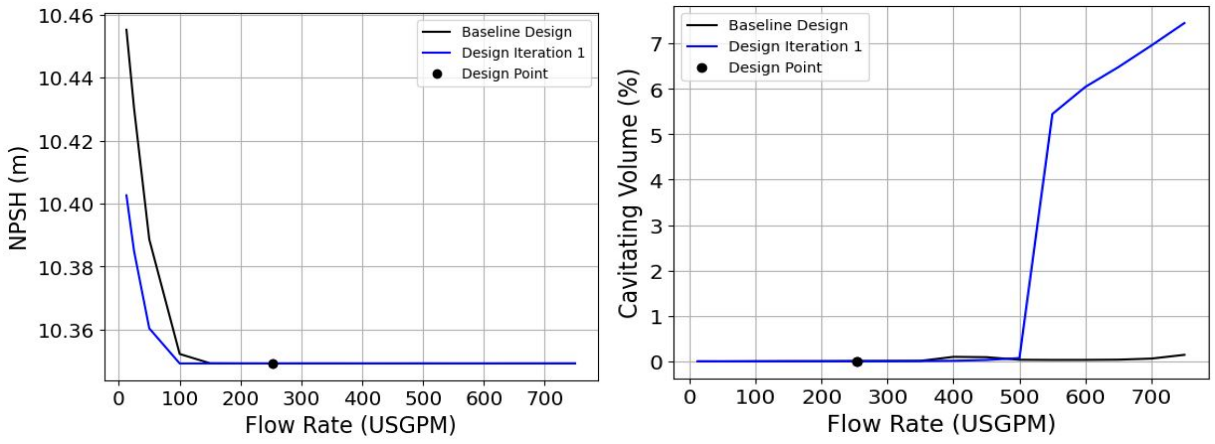

(a) (b)

Figure 4.8: Cavitation in the two designs expressed as (a) NPSH (m) and (b) Cavitating volume (%)

Table 4.1: Performance characteristics of the three designs at the operating point

Performance features	**Baseline design**	**Design iteration 1**	**Design iteration 2**
Head, m	96.15	96.66	98.04
Efficiency %	52.25	65.38	67.73
Power, W	28761.9	23100.2	22619.8

the losses incurred in the volute for the two cases are almost the same. This is further illustrated in Figure 4.10. Figure 4.10a shows that there is almost a vertical shift of the curve, *i.e.* the head delivered by the impeller of the second iteration design has increased for all flow rates by almost the same margin. However, there is no significant difference in head loss incurred in volute between the two designs. Hence, it should not be surprising that there is vertical shift in the head-capacity curve for second iteration design relative to that for the first iteration design. In the turbomachinery terminology, this implies that the slip factor has increased, *i.e.* the flow is more blade-congruent.

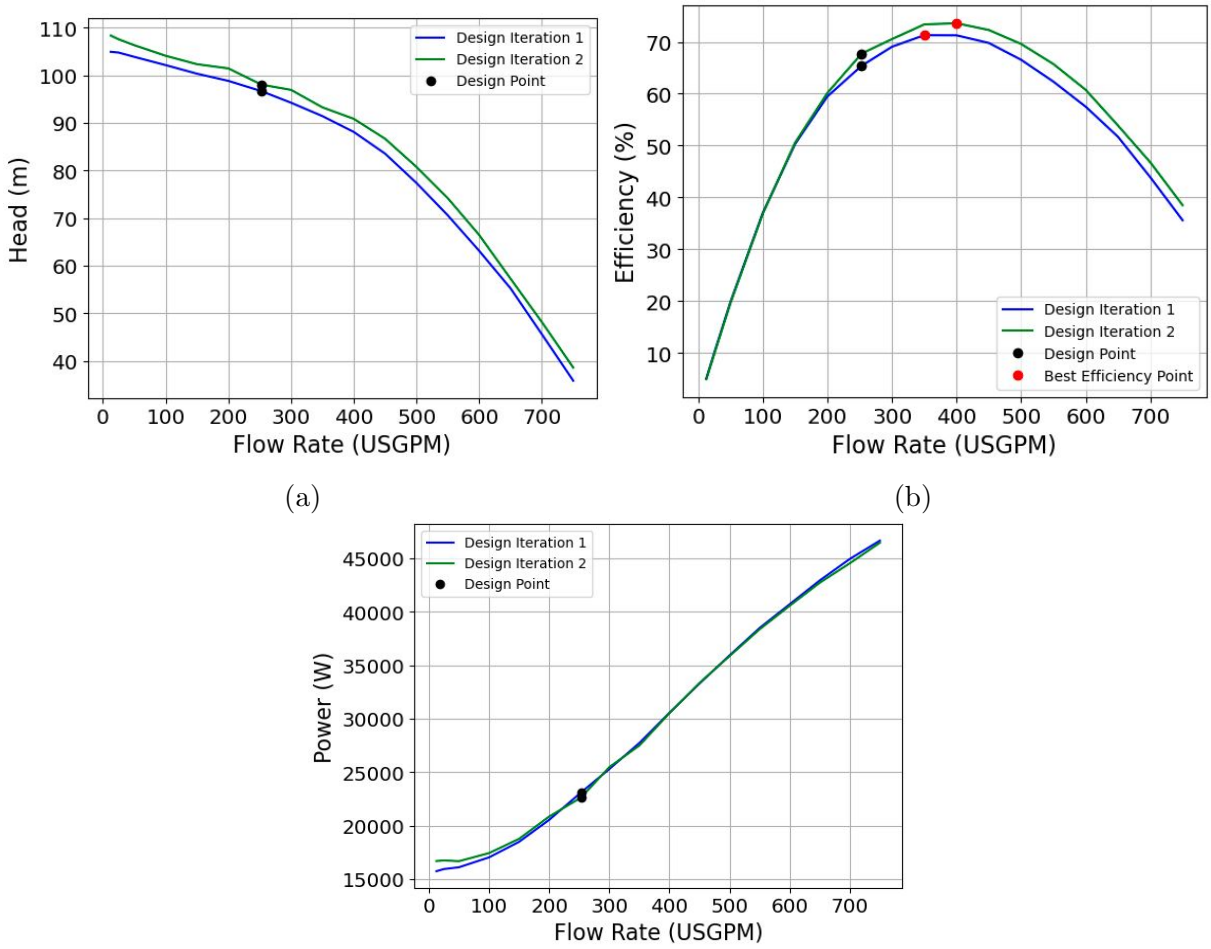

Figure 4.9: Performance characteristics resulting from reduction in volute throat area and gap width of the baseline design in comparison to those of the first iteration design

4.5 Volute with Axial Diffuser

The performance characteristics discussed thus far correspond to a pump with a tangential diffuser. Another common volute used in pumps has an axial diffuser. The two designs are shown in Figure 4.11. There have been studies done comparing the performance characteristics of the two designs. A numerical study done by Alemi et al. [1] showed that the pump with the axial diffuser in the low-specific speed range has slightly better efficiency

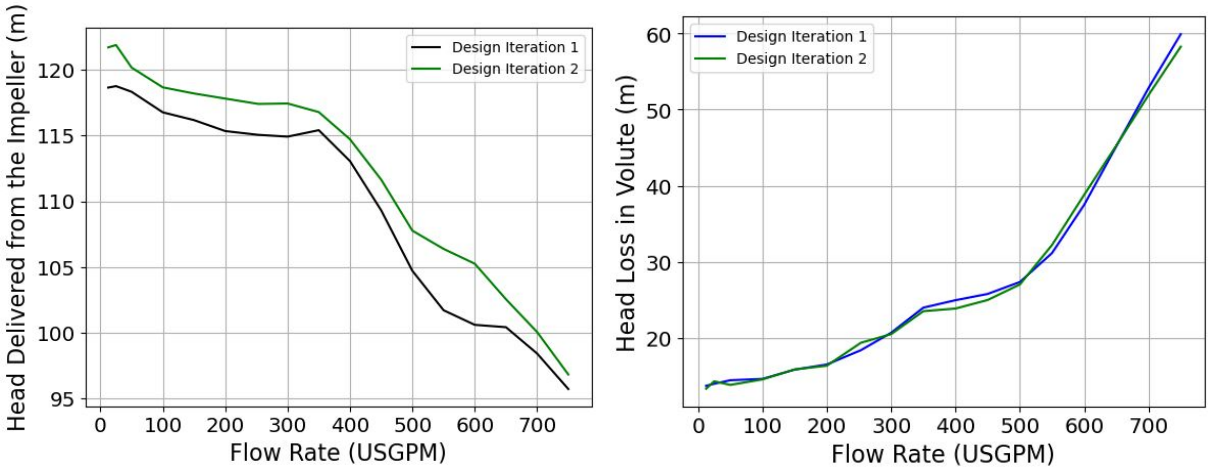

(a) (b)

Figure 4.10: (a) Head delivered from the impeller and (b) Head loss in volute for the two designs

at the design point and higher flow rates, while the head delivered was almost the same for both cases. However, the same conclusion could not be drawn from the numerical study of the pump under consideration, with the tangential diffuser being replaced with an axial diffuser.

The numerical study of the pump with axial volute involved the same design iterations that were done for the pump with tangential volute. The performance characteristics of the baseline case with axial diffuser compared to those of the same case with tangential diffuser are shown in Figure 4.12. No significant differences in performance characteristics were observed at the design point. The head output is slightly higher at the design point and the part load for the case with axial diffuser in comparison to that produced by the baseline design with tangential diffuser. However, the trend reverses for overload conditions, where the difference is more pronounced compared to that observed at underload conditions. The efficiency of the design with an axial diffuser is also lower than that of the design with a tangential diffuser under overload conditions. This difference can be attributed to the viscous losses in the volute shown in Figure 4.12d for each design. When the same impeller was used for both designs, the head generated by the impeller at the impeller outlet was almost the same for both cases. However, the flow in volute with axial diffuser suffers from greater head loss relative to that in volute with tangential diffuser, and the difference only increases as the flow rate increases. The power requirements are almost the same at all flow rates. Therefore, for the baseline case, Figure 4.12 shows that the volute with the

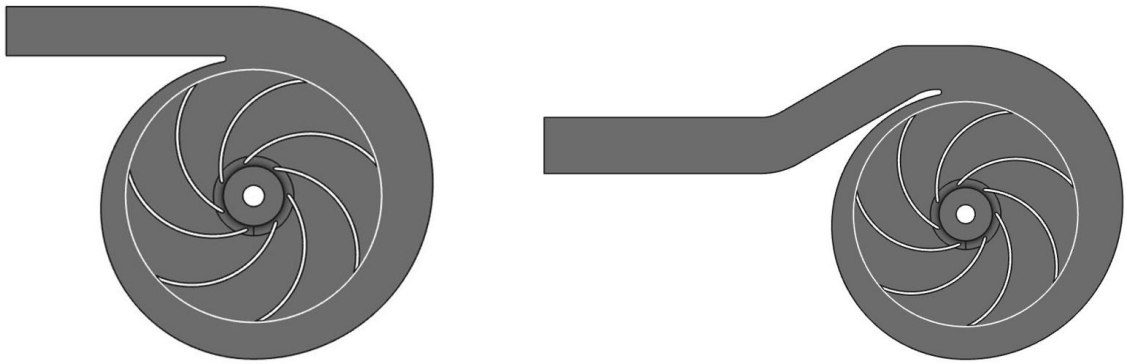

(a) (b)

Figure 4.11: (a) Pump with tangential volute and (b) Pump with axial volute

tangential diffuser gives superior performance. The numerical simulations of the cases with reduced throat area and reduced gap width yielded the same conclusion. If anything, the effect was observed to be more pronounced in these cases.

Figure 4.13 shows the performance features of the first iteration design for both cases. As with the baseline case, there has been no significant change in the performance features at the design point. However, the difference in the head-capacity curves for the two cases at overload conditions is more eminent than that observed for the baseline case. The same conclusion can be drawn for the efficiency curves. Once again, the reason can be attributed to head losses in the volute shown in Figure 4.13d for each case. Compared to Figure 4.12d, the difference in head losses is more pronounced under overload conditions. The maximum difference in head losses in Figure 4.12d is 3.02 m at 700 USGPM, while the difference in head losses at the same flow rate for the first iteration design is 18.76 m. Therefore, the impact of the volute with the axial diffuser becomes more pronounced at overload conditions as the volute throat area is reduced.

The study was further extended to study the performance characteristics of the second iteration design with different volute types. The results were very similar to those obtained for the first iteration design, shown in Figure 4.13. The differences in head losses were slightly higher than those shown in Figure 4.13d. Therefore, the effect of the axial diffuser becomes slightly more pronounced compared to that shown in Figure 4.13 as the gap width is reduced of the first iteration design.

In view of the results shown thus far for the pump with an axial diffuser in comparison to that with a tangential diffuser, the pump with the tangential diffuser seems to yield better performance characteristics overall. However, this conclusion cannot be generalized.

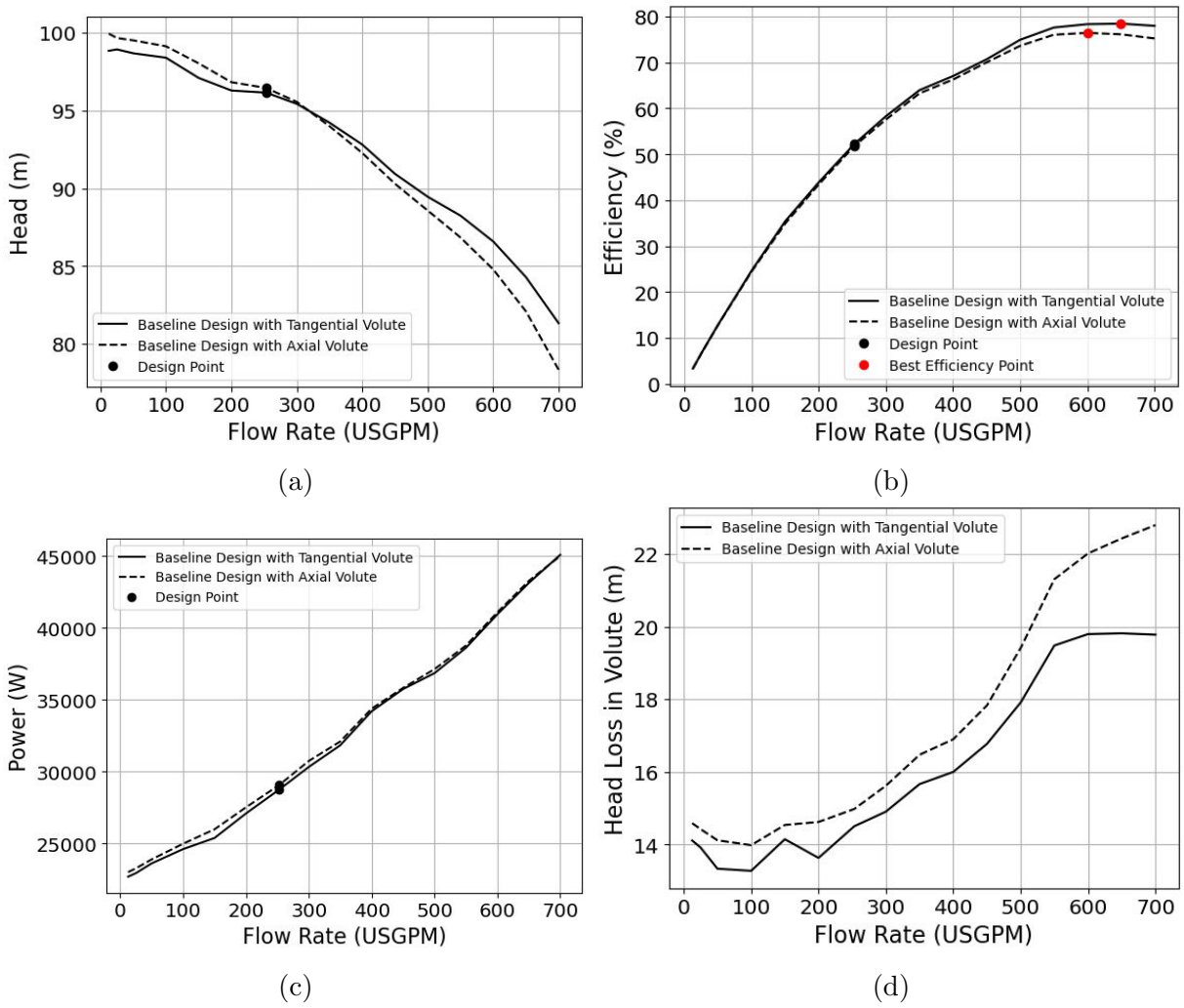

Figure 4.12: Performance characteristics of the baseline design with axial volute in comparison to those of the same design with tangential volute

As mentioned above, another study done showed that the pump with an axial diffuser yielded better performance characteristics at the design flow rate and overload conditions [1]. The conclusion that can be made here is that the impact of the axial diffuser compared to that of the tangential diffuser depends on the particular pump geometry being studied.

The conclusions made thus far are based on the performance features shown in numerous plots. A number of these plot show hydraulic losses in volute as a function of

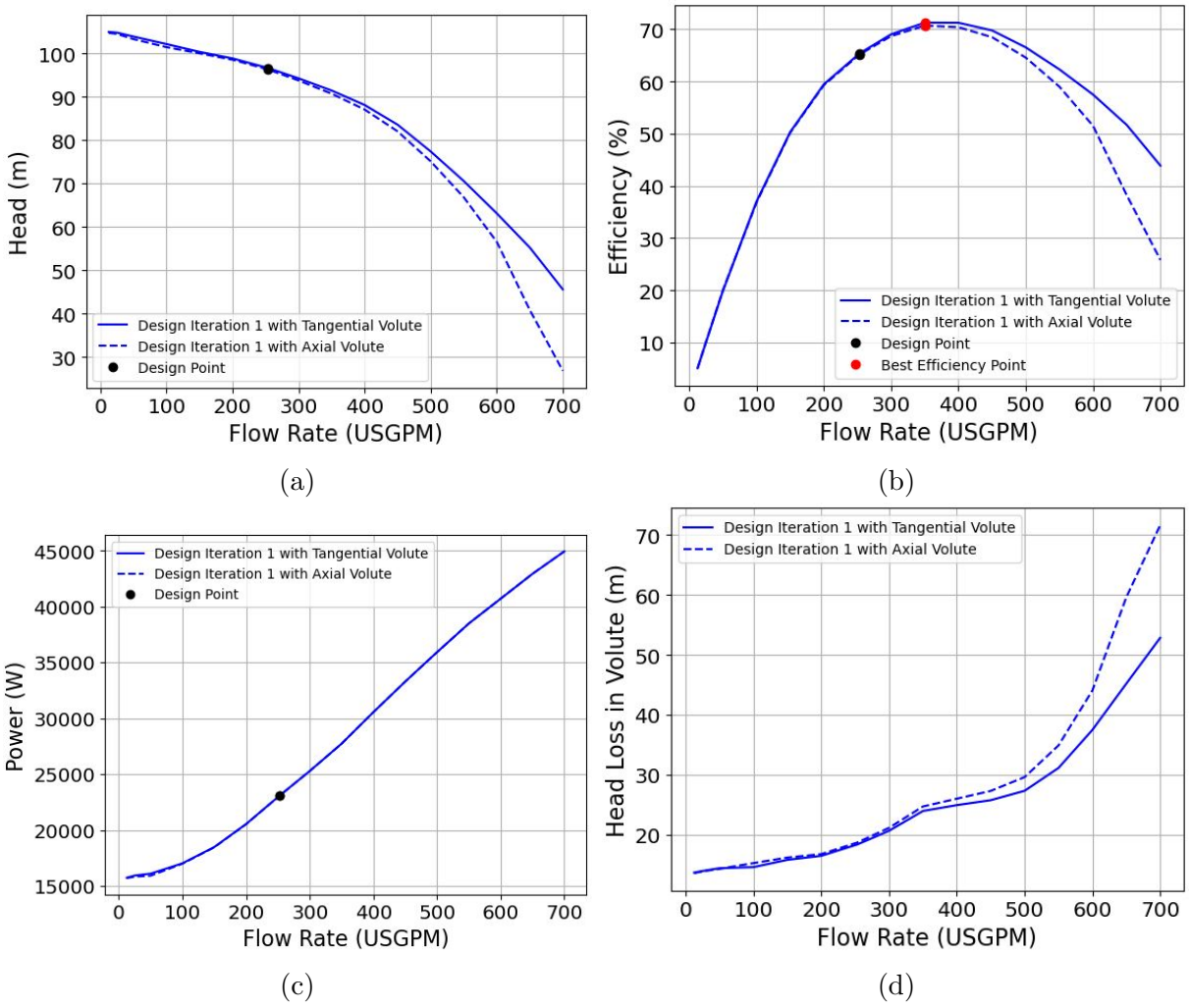

Figure 4.13: Performance characteristics of the first iteration design with axial volute in comparison to those of the same design with tangential volute

flow rate (Figures 4.7b, 4.10b, 4.12d, and 4.13d). These figures can reveal a lot about the performance characteristics of the pump on close investigation. For example, the point of inflection for each plot (baseline case and first iteration design) in Figure 4.7b occurs at the BEP of the design. The same is the case for Figure 4.10b, where inflection points in the curve can be seen at BEP of the respective designs. Furthermore, the triangle-shaped feature of the plot for volute losses for the baseline design that is observed in Figure 4.12d covers the range of flow rates where there is slight instability in the head-capacity curve

for the same design. This shows the significant impact volute can have on the performance features of the pump.

Volute can have a significant impact on the performance features of the pump, but so can an impeller. It is worthwhile to investigate the effect on performance characteristics with an unconventional impeller design commonly used for low-specific speed application, *i.e.* the radial bladed impeller.

4.6 Radial Bladed Impeller

As discussed in section 2.3.1, the radial bladed impeller was developed to cater for low-specific speed applications. The radial blade design, *i.e.* the blade with an inlet and outlet angles of 90°, results in a higher head delivered than can be delivered from a conventionally designed impeller. The head delivered has been shown to increase with the angle of release of the blade [12]. An additional benefit of this design is that it allows for a much greater number of blades to be used than the number of blades used in a conventionally designed impeller. This further contributes to increasing the head delivered. Both the blade outlet angle and number of blades are directly related to the head delivered by the impeller according to equation (3.22). The greater number of blades ensures less flow deviation towards the outlet, *i.e* higher slip factor, which further contributes to increasing the head delivered.

Although the radial bladed design is known to significantly increase the head delivered relative to the head delivered from a conventionally designed impeller, this comes at a cost. A common downside to the radial bladed impeller that has been shown in several studies is the instability in the head-capacity curve near shut-off point [13, 20]. The radial bladed impeller is commonly used as a semi-open impeller, *i.e.* it has no shroud and just a hub built into it. With just a hub, it is possible to have blades on either side, which can significantly increase the number of blades and, hence, the head delivered. This impeller is often referred to as a double-acting impeller [18] and can deliver head well over 300 m [18]. A typical double-acting impeller is shown in Figure 4.14. The holes in the hub wall are referred to as balance holes, which allow the fluid flow to the rear side of the pump to make effective use of the blades on either side. However, there are some downsides to this impeller design.

As expected, such an impeller design substantially increases the power requirements. Additionally, with such designs, an additional parameter becomes an important influence on the performance characteristics, *i.e.* the tip clearance. As discussed in section 2.2, the

Figure 4.14: A typical design of a double-acting impeller (source: [38])

performance features of low-specific speed pumps are known to be sensitive to tip clearance [5], which is the gap between the casing cover and the tip of the blades. These designs also involve significant volumetric losses, which is detrimental to overall efficiency of the pump.

In view of these issues, the radial bladed impeller was studied as a closed impeller with the same tangential volute design used for the first iteration design. As mentioned, radial bladed impellers are known to exhibit instability near the shut-off point. The volute with reduced throat area makes the head-capacity curve steeper, and hence, was thought to stabilize the head-capacity features. However, as will be shown, this did not work as was intended. As a starting point, the number of blades was chosen to be 12. The performance characteristics obtained are shown in Figure 4.15.

Figure 4.15 shows that there is significant instability in the head-capacity curve at underload conditions. This makes this design undesirable if operating underload. The head output at design point has significantly increased compared to that obtained from other designs. The other design options investigated so far yielded head output close to 100 m at the design point, whereas the radial bladed impeller design yielded the head output of 120.5 m at the same point, *i.e* an increase of around 20 m. However, the significant instability in the head-capacity curve means that this design has a much narrower range of operation compared to the other designs. The efficiency at the design point is comparable to that obtained for the baseline design at the same flow rate. However, as expected, power requirements have increased significantly. Of all the designs investigated so far, the

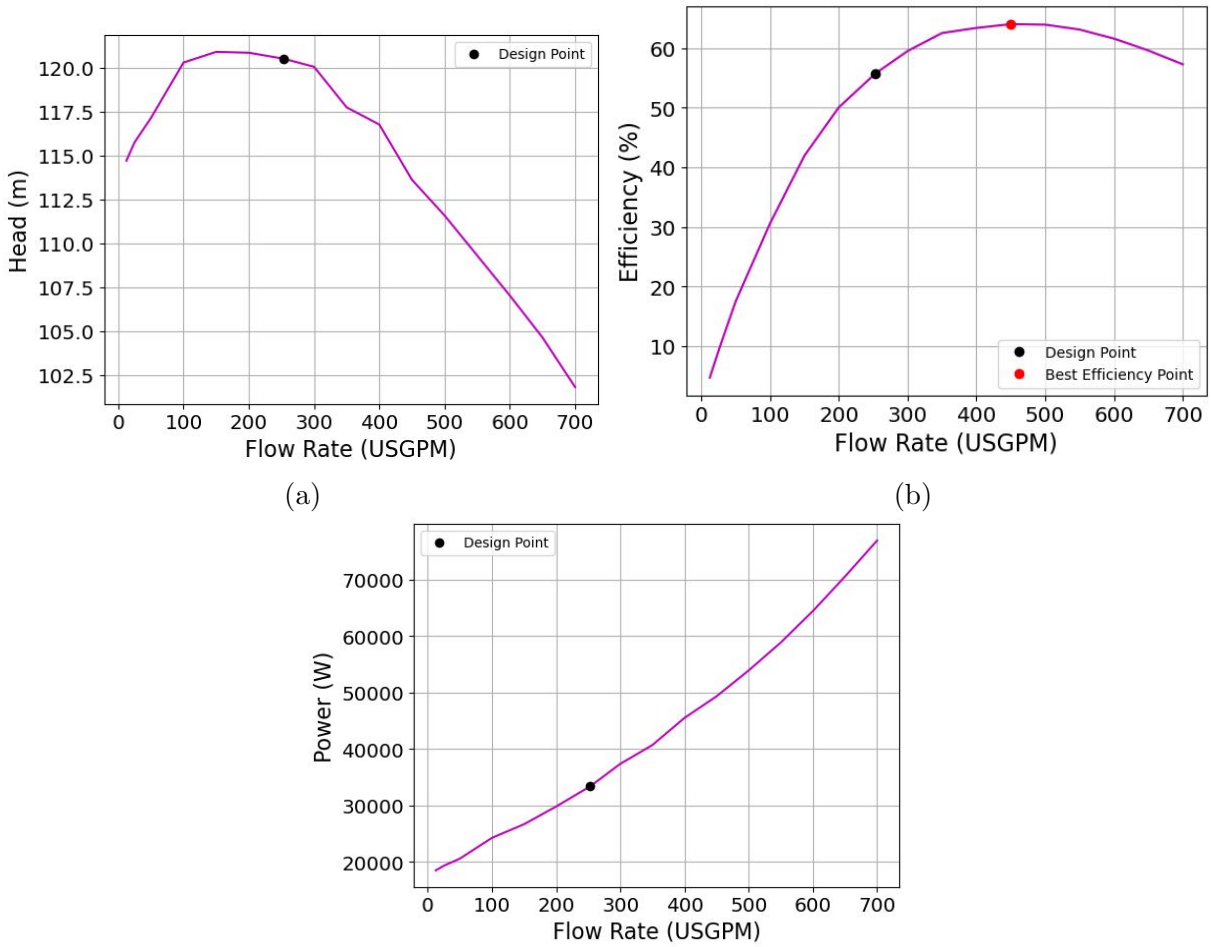

Figure 4.15: Performance characteristics of the radial bladed impeller with tangential volute

baseline design has the highest power requirements at the design point (28, 762 W for the design with tangential volute and 29, 080 W for the design with axial volute). With the radial bladed impeller, the power required is 33, 379 W at the same flow rate. The power required will increase even further as the number of blades are increased.

The same design was modified to increase the number of blades to 15, while other design features were kept the same. This results in even greater instability in the head-capacity curve and hence further reduced the range of operation. Furthermore, as expected, the

power requirements also showed an increase from what is shown in Figure 4.15c. These issues can be resolved by reducing the number of blades. However, in such a case, the performance characteristics of the radial bladed impeller will become similar to those of the baseline design. Additionally, with radial blades, it is important to have more blades than the number of blades used in conventional design. If the radial bladed impeller is designed with the same number of blades as used for conventional design, *i.e.* 5 to 7, there is significant room for flow deviation towards the impeller outlet. This implies that the slip factor can significantly get reduced, which, in turn, will reduce the head output.

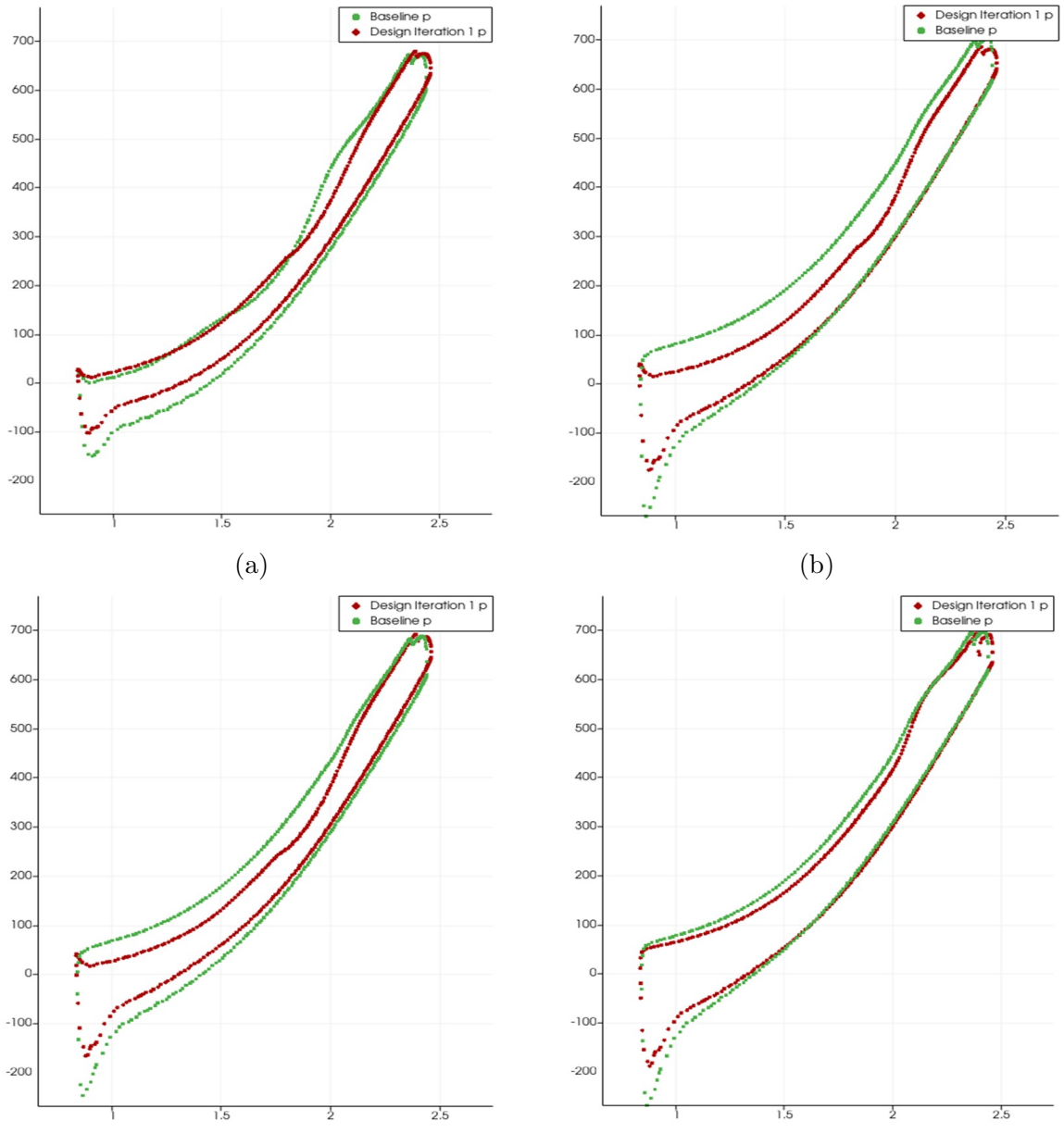

Figure 4.16: Pressure distribution in Pascals over the pressure and suction sides of the blade in streamwise direction at a discharge rate of (a) 100 USGPM, (b) 253 USGPM, (c) 400 USGPM, and (d) 600 USGPM.

Chapter 5

Conclusions and Recommendations

The work carried out relates to the design and optimization of the centrifugal pump for low-specific speed applications. A property used to define the design of the pumps is the specific speed, which relates the flow properties of the pump at its operating point. Pumps of lower specific speed are particularly interesting because they yield a high value of head (representative of mechanical energy) at a relatively low flow rate. This reduces the power requirements required to operate the shaft that rotates the impeller. A design strategy that uses a combination of empirical relations based on experimental measurements and theory is used to define a baseline design intended to operate at a flow rate of 253 USGPM. The performance of the design is evaluated based on the head-capacity curve, efficiency, and power requirements. These performance characteristics are obtained using numerical simulations that involved the solution of the Reynolds Averaged Navier-Stokes (RANS) equations using the SST $k - \omega$ model.

Designs with a tangential diffuser were first simulated. Performance features of the baseline case had some undesirable features. There was slight instability (positive slope) observed near the shut-off point. Additionally, the BEP (Best Efficiency Point) was located at a much higher discharge than the design flow rate. It is important to have a BEP close to the design flow rate, so that the efficiency of the operating point of the pump is closer to that of the BEP. The performance features were improved by reducing the volute throat area by 50% (referred to as the first iteration design). This resulted in the BEP being shifted much closer to the design point and the head-capacity curve becoming much steeper compared to that of the baseline case. The difference between the design point and BEP for the first iteration design was observed to be around 100 USGPM, as opposed to about 400 USGPM observed for the baseline case. The efficiency of the design point also improved by about 13% compared to that for the baseline case. Power requirements decreased significantly

for the flow rate of up to 500 USGPM for the first iteration design, which contributed to the improvement in efficiency up to the flow rate of about 450 USGPM. Past this flow rate, the efficiency of the first iteration design is lower than those of the baseline design. The investigation of the internal flow fields reveal that viscous effects become a lot more significant for the first iteration design at overload conditions (flow past 400 USGPM) than those observed for the baseline case under the same conditions, leading to a dramatic pressure drop towards the outlet. This significantly reduces the head value produced under these conditions and reduces the efficiency. This is why the head-capacity curve for the first iteration design is much steeper compared to that for the baseline design.

An even further improvement was achieved by reducing the gap width of the volute by 50% in addition to the reduction in the throat of the volute (referred to as the second iteration design). This resulted in the head-capacity curve being shifted vertically upwards, *i.e.* the head delivered increased for all flow rates by almost the same margin compared to that delivered from the first iteration design. At the design point, the head delivered increased from 96.66 m for the first iteration design to 98.04 m for the second iteration design. The efficiency also improved by 2.34%. However, no significant changes were observed in the power requirements. It was revealed that this effect was due to the increase in the slip factor, *i.e.* the flow become more blade congruent for all flow rates as a result of the gap width being reduced.

The same design iterations were performed for the case of axial diffuser. Although no significant differences in performance features were observed at underload and design conditions between the two corresponding designs, the head delivered and efficiency noticeably decreased at overload conditions. It was observed that this was due to increased viscous losses in the volute with the axial diffuser compared to the one with tangential diffuser under overload conditions for all design iterations. This leads to significant head losses under overload conditions. Overall, the design with tangential volute performed better.

A design with radial bladed impeller and tangential volute was also simulated. The radial-bladed impeller is particularly suited to low-specific speed applications because it tends to yield higher head output than that delivered from the conventionally designed impeller. The head delivered at the design point for this case increased to more than 120 m. However, this came at the cost of a significant instability observed at partload conditions. Additionally, the power requirements also increased substantially in this case. Significant instability at partload conditions means that the pump has a narrower range of operation and cannot be operated at flow rates lower than the design flow rates.

Moving forward, a logical step would be to look into optimizing the radial-bladed impeller so that there is instability at partload. This can be beneficial because radial

blades deliver significantly more head output than the conventionally designed backward bent blades at all flow rates.

Two aspects not investigated in detail in this study are hydraulic forces and rotor-stator interactions. It would be interesting to see how the unsteady flow structures released at the impeller outlet and their evolution change as the volute throat area and gap width is reduced. Rotor-stator interaction becomes more intense with the reduction in throat area and gap width, and it would be interesting to investigate this in detail by studying the unsteady flow structures. Reduction in gap width is expected to result in higher pressure pulsations near the tongue region of the volute, which will increase the radial force experienced by the impeller. This can also be investigated in the future.

Another aspect that has been widely used in recent times is the integration of optimization algorithms with Computational Fluid Dynamics (CFD). This results in a powerful workflow that navigates through different design options defined by the geometrical constraints to locate the one that optimizes the objective function. This can be used to maximize the efficiency, head, or minimize cavitation. The workflow can even involve multiple-objective optimization that locates the Pareto-optimal designs. The author has worked to develop a parametric model of the pump shown in Appendix A that he intends to use for optimization study in near future.

References

[1] Hamed Alemi, Seyyed Ahmad Nourbakhsh, Mehrdad Raisee, and Amir Farhad Najafi. Effects of volute curvature on performance of a low specific-speed centrifugal pump at design and off-design conditions. *Journal of Turbomachinery*, 137(4):041009, 2015.

[2] Ravi Balasubramanian, Simon Bradshaw, Eugene Sabini, et al. Influence of impeller leading edge profiles on cavitation and suction performance. In *Middle East Turbomachinery Symposia. 2013 Proceedings.* Turbomachinery Laboratory, Texas A&M Engineering Experiment Station, 2013.

[3] UM Barske. Development of some unconventional centrifugal pumps. *Proceedings of the Institution of Mechanical Engineers*, 174(1):437–461, 1960.

[4] W Beekman and R Asdal. Improving pumping system performance a sourcebook for industry, 2006.

[5] G Boitel, D Fedala, and N Myon. Tip clearance effects on loads and performances of semi-open impeller centrifugal pumps at different specific speeds. In *IOP Conference Series: Earth and Environmental Science*, volume 49, page 032013. IOP Publishing, 2016.

[6] Hermod Brekke. Pumps and turbines. *NTNU Water Power Laboratory, Trondheim, Norway*, 2003.

[7] Christopher E Brennen. *Hydrodynamics of pumps*. Cambridge University Press, 2011.

[8] José A Caridad and Frank Kenyery. Slip factor for centrifugal impellers under single and two-phase flow conditions. *Journal of Fluids Engineering*, 2005.

[9] Lilian Chabannes, David Štefan, and Pavel Rudolf. Effect of splitter blades on performances of a very low specific speed pump. *Energies*, 14(13):3785, 2021.

[10] Lilian Chabannes, David Štefan, and Pavel Rudolf. Volute throat area and wall modelling influence on the numerical performances of a very low specific speed pump. In *IOP Conference Series: Earth and Environmental Science*, volume 774, page 012007. IOP Publishing, 2021.

[11] Young-Do Choi, Junichi Kurokawa, and Jun Matsui. Performance and internal flow characteristics of a very low specific speed centrifugal pump. 2006.

[12] Baoling Cui, Canfei Wang, Zuchao Zhu, and Yingzi Jin. Influence of blade outlet angle on performance of low-specific-speed centrifugal pump. *Journal of Thermal Science*, 22(2):117–122, 2013.

[13] Trygve Dahl et al. Centrifugal pump hydraulics for low specific speed applications. In *Proceedings of the 6th international pump users symposium*. Turbomachinery Laboratories, Department of Mechanical Engineering, Texas A&M . . . , 1989.

[14] Brad Falck, Daniel Falck, and Brad Collette. *Freecad [How-To]*. Packt Publishing Ltd, 2012.

[15] Bo Gao, Pengming Guo, Ning Zhang, Zhong Li, and MinGuan Yang. Unsteady pressure pulsation measurements and analysis of a low specific speed centrifugal pump. *Journal of Fluids Engineering*, 139(7), 2017.

[16] Bo Gao, Ning Zhang, Zhong Li, Dan Ni, and MinGuan Yang. Influence of the blade trailing edge profile on the performance and unsteady pressure pulsations in a low specific speed centrifugal pump. *Journal of Fluids Engineering*, 138(5), 2016.

[17] Edward M Greitzer. The stability of pumping systems—the 1980 freeman scholar lecture. 1981.

[18] Johann Friedrich Gülich. *Centrifugal pumps*, volume 2. Springer, 2008.

[19] Andrew Jackson. A comprehensive tour of snappyhexmesh. In *7th OpenFOAM workshop*, volume 596, 2012.

[20] Shusaku Kagawa and Junichi Kurokawa. New centrifugal pump in very low specific speed range. In *Fluids Engineering Division Summer Meeting*, volume 44403, pages 89–96, 2011.

[21] Shin-Hyoung Kang, Woon-Je Cho, Hayong Yun, and Seungkap Lee. Performance variations of small centrifugal compressor with exit blade thickness. pages 135–141, 1998.

[22] Igor J Karassik, Joseph P Messina, Paul Cooper, and Charles C Heald. *Pump handbook*. McGraw-Hill Education, 2008.

[23] Jens Keller, Eduardo Blanco, Raúl Barrio, and Jorge Parrondo. Piv measurements of the unsteady flow structures in a volute centrifugal pump at a high flow rate. *Experiments in fluids*, 55:1–14, 2014.

[24] Hye In Kim, Tae-Seong Roh, Hwanil Huh, and Hyoung Jin Lee. Development of ultra-low specific speed centrifugal pumps design method for small liquid rocket engines. *Aerospace*, 9(9):477, 2022.

[25] Roman Klas, František Pochylỳ, and Pavel Rudolf. Analysis of novel low specific speed pump designs. In *IOP Conference Series: Earth and Environmental Science*, volume 22, page 012010. IOP Publishing, 2014.

[26] Junichi Kurokawa, Kazunari Matsumoto, Jun Matsui, and Hiroshi Imamura. Development of high efficiency volute pump of very low specific speed. In *Proceedings of the 6th Asian International Conference on Fluid Machinery (Johor, Malaysia)*, pages 250–255, 2001.

[27] Florian R Menter. Two-equation eddy-viscosity turbulence models for engineering applications. *AIAA journal*, 32(8):1598–1605, 1994.

[28] FR Menter. Multiscale model for turbulent flows. In *24th fluid dynamics conference. American Institute of Aeronautics and Astronautics*, volume 30, pages 198–214, 1993.

[29] Lev Nelik. *Centrifugal & rotary pumps: fundamentals with applications*. CRC press, 1999.

[30] Grunde Olimstad, Morten Osvoll, and Pål Henrik Enger Finstad. Very low specific speed centrifugal pump—hydraulic design and physical limitations. *Journal of Fluids Engineering*, 140(7), 2018.

[31] Jorge L Parrondo, Sandra Velarde, and Carlos Santolaria. Development of a predictive maintenance system for a centrifugal pump. *Journal of Quality in Maintenance Engineering*, 1998.

[32] Nicholas Pedersen. Experimental investigation of flow structures in a centrifugal pump impeller using particle image velocimetry. *Technical University of Denmark*, 2000.

[33] C Pfleiderer. Centrifugal pump for liquids and gases, 1949.

[34] George Frederick Round. *Incompressible flow turbomachines: design, selection, applications, and theory*. Elsevier, 2004.

[35] Hiroshi Satoh, Kazuo Uchida, Yinchun Cao, et al. Designing an ultra-low specific speed centrifugal pump. In *Proceedings of the 22nd International Pump Users Symposium*. Texas A&M University. Turbomachinery Laboratories, 2005.

[36] Mario Šavar, Hrvoje Kozmar, and Igor Sutlović. Improving centrifugal pump efficiency by impeller trimming. *Desalination*, 249(2):654–659, 2009.

[37] CFD SUPPORT S.R.O. *TCAE Manual Version 21.09*, 2021.

[38] Alexey Joakim Stepanoff. Centrifugal and axial flow pumps. *Theory, Design, and Application*, 1957.

[39] Ran Tao, Ruofu Xiao, and Zhengwei Wang. Influence of blade leading-edge shape on cavitation in a centrifugal pump impeller. *Energies*, 11(10):2588, 2018.

[40] Henk Kaarle Versteeg and Weeratunge Malalasekera. *An introduction to computational fluid dynamics: the finite volume method*. Pearson education, 2007.

[41] Yangyang Wei, Yang Yang, Ling Zhou, Lei Jiang, Weidong Shi, and Gaoyang Huang. Influence of impeller gap drainage width on the performance of low specific speed centrifugal pump. *Journal of Marine Science and Engineering*, 9(2):106, 2021.

[42] RW Westra, L Broersma, Koen van Andel, and Nicolaas P Kruyt. Piv measurements and cfd computations of secondary flow in a centrifugal pump impeller. *Journal of fluids engineering*, 132(6), 2010.

[43] FJ Wiesner. A review of slip factors for centrifugal impellers. 1967.

[44] David C Wilcox. Multiscale model for turbulent flows. *AIAA journal*, 26(11):1311–1320, 1988.

[45] Zhenfa Xu, Fanyu Kong, Lingfeng Tang, Mingwei Liu, Jiaqiong Wang, and Ning Qiu. Effect of blade thickness on internal flow and performance of a plastic centrifugal pump. *Machines*, 10(1):61, 2022.

[46] Sunsheng Yang, Fanyu Kong, and Bin Chen. Research on pump volute design method using cfd. *International Journal of Rotating Machinery*, 2011, 2011.

[47] Ning Zhang, Bo Gao, Zhong Li, Dan Ni, and Qifeng Jiang. Unsteady flow structure and its evolution in a low specific speed centrifugal pump measured by piv. *Experimental thermal and fluid science*, 97:133–144, 2018.

[48] Ning Zhang, Minguan Yang, Bo Gao, Zhong Li, and Dan Ni. Investigation of rotor-stator interaction and flow unsteadiness in a low specific speed centrifugal pump. *Strojniški vestnik-Journal of Mechanical Engineering*, 62(1):21–31, 2016.

APPENDICES

Appendix A

Python Code for development of Parametric Model of Pump

```
# Script creates a Centrifugal pump. Impeller is created using circular arc method.
# Cutwater is created using circular arc
# all dimensions are in mm
# the script was meant to used to optimize the hydraulic performance of the pump. Hence, the sidewall gaps are not considered


import Part, FreeCAD, Mesh, MeshPart

class Pump:
  def __init__(self, obj):
     obj.Proxy = self
     obj.addProperty("App::PropertyFloat", "R0", "Dimensions", "Radius of an impeller").R0=_R0_
     obj.addProperty("App::PropertyFloat", "R1", "Dimensions", "Inlet Radius of a shroud").R1=49
     obj.addProperty("App::PropertyFloat", "R2", "Dimensions", "Inlet Radius of a hub").R2=17.5
     obj.addProperty("App::PropertyFloat", "R3", "Dimensions", "Radius of shroud curvature").R3=16
     obj.addProperty("App::PropertyFloat", "b", "Dimensions", "Width of a outlet").b=_b_
     obj.addProperty("App::PropertyFloat", "L0", "Dimensions", "Length of Inlet Pipe").L0=196
     obj.addProperty("App::PropertyFloat", "L1", "Dimensions", "Horizontal
```

```
    length of the shroud/hub").L1=11
19   obj.addProperty("App::PropertyFloat", "t", "Dimensions", "Thickness
    of Blades").t=6
20   obj.addProperty("App::PropertyFloat", "theta_1", "Dimensions", "Blade
     Inlet Angle").theta_1=35
21   obj.addProperty("App::PropertyFloat", "theta_2", "Dimensions", "Blade
     Outlet Angle").theta_2=_theta_2_
22   obj.addProperty("App::PropertyFloat", "L2", "Dimensions", "Length of
    Construction Line").L2=35
23   obj.addProperty("App::PropertyFloat", "Z", "Dimensions", "Number of
    blades").Z=7
24   obj.addProperty("App::PropertyFloat", "L3", "Dimensions", "Shroud/Hub
     thickness").L3=3
25   obj.addProperty("App::PropertyFloat", "L4", "Dimensions", "Gap width
    for volute").L4=9
26   obj.addProperty("App::PropertyFloat", "L5", "Dimensions", "Dimension
    corresponding to volute throat area").L5=42
27   obj.addProperty("App::PropertyFloat", "L6", "Dimensions", "Dimension
    corresponding to 75% volute throat area").L6=32
28   obj.addProperty("App::PropertyFloat", "L7", "Dimensions", "Dimension
    corresponding to 50% volute throat area").L7=21
29   obj.addProperty("App::PropertyFloat", "L8", "Dimensions", "Dimension
    corresponding to 25% volute throat area").L8=11
30   obj.addProperty("App::PropertyFloat", "theta_3", "Dimensions", "Angle
     of CutWater").theta_3=12.5
31   obj.addProperty("App::PropertyFloat", "R4", "Dimensions", "Diameter
    of CutWater").R4=10
32   obj.addProperty("App::PropertyFloat", "L9", "Dimensions", "Length of
    Outlet").L9=400
33   obj.addProperty("App::PropertyFloat", "R5", "Dimensions", "Radial
    Distance from the inlet to the leading edge position of the blades").
    R5=6
34
35 def execute (self, obj):
36   from math import pi
37
38   export_dir_imp = u"STL/Impeller/"
39   export_dir_inlet = u"STL/Inlet/"
40   export_dir_volute = u"STL/Volute/"
41
42   # Creation of blades using circular arc method
43
44   # creation of inlet and outlet construction circles
45   circle_out_cons = Part.makeCircle(obj.R0-2, FreeCAD.Vector(obj.L0+obj
    .L1+obj.R3, 0, 0), FreeCAD.Vector(1, 0, 0))
```

```
46      circle_in_cons = Part.makeCircle(obj.R1+obj.R5, FreeCAD.Vector(obj.L0
    +obj.L1+obj.R3, 0, 0), FreeCAD.Vector(1, 0, 0))
47      #Part.show(circle_out_cons)
48      #Part.show(circle_in_cons)
49
50      # creation of outlet construction line used for defining the outlet
    angle
51      outlet_cons_line = Part.LineSegment(FreeCAD.Vector(obj.L0+obj.L1+obj.
    R3, obj.R0-2, 0), FreeCAD.Vector(obj.L0+obj.L1+obj.R3, obj.R0-2, obj.
    L2)).toShape()
52      outlet_cons_line.rotate(FreeCAD.Vector(obj.L0+obj.L1+obj.R3, obj.R0
    -2, 0), FreeCAD.Vector(1, 0, 0), 360-obj.theta_2)
53      #Part.show(outlet_cons_line)
54
55      # Creation of inlet construction line used for defining the inlet and
        outlet angles of the blades
56      Inlet_cons_line = Part.LineSegment(FreeCAD.Vector(obj.L0+obj.L1+obj.
    R3, 0, 0), FreeCAD.Vector(obj.L0+obj.L1+obj.R3, obj.R1+obj.R5, 0)).
    toShape()
57      Inlet_cons_line.rotate(FreeCAD.Vector(obj.L0+obj.L1+obj.R3, 0, 0),
    FreeCAD.Vector(1, 0, 0), 360-(obj.theta_1 + obj.theta_2))
58
59      # this line joins the outlet construction line to the inlet
    construction line at the inlet construction circle
60      le_cons_line_1 = Part.LineSegment(outlet_cons_line.Vertexes[0].Point,
        Inlet_cons_line.Vertexes[1].Point).toShape()
61      slope_le_cons_line_1 = (outlet_cons_line.Vertexes[0].Point-
    Inlet_cons_line.Vertexes[1].Point).normalize()
62
63      # the slope of the line (le_cons_line_1) is used to establish an
    another point in the same direction extended beyond the inlet
    construction circle
64      dummy_point_1 = FreeCAD.Vector(-slope_le_cons_line_1.multiply(
    le_cons_line_1.Length+obj.R1))+outlet_cons_line.Vertexes[0].Point
65
66      # this line joins the vertex of the outlet construction line to the
    point established in the last line of code so that the line
    intersects the inlet construction circle at two points (the second of
        which is the leading edge)
67      le_cons_line_2 = Part.LineSegment(outlet_cons_line.Vertexes[0].Point,
        dummy_point_1).toShape()
68      #Part.show(le_cons_line_2)
69
70      intersect_le_point = le_cons_line_2.Curve.intersect(circle_in_cons.
    Curve)[0].toShape().Point
```

```
71
72      # camber line for the blade profile (represented as circular arc)
73      cir_arc = Part.Arc(intersect_le_point, outlet_cons_line.Vertexes[0].
    Point, outlet_cons_line.Vertexes[1].Point).toShape()
74      #Part.show(cir_arc)
75
76      # center of ellipse
77      ell_cen = cir_arc.valueAt(cir_arc.getParameterByLength(obj.t))
78
79      # unit normal direction at the center of ellipse
80      normal_dir_cen_ell = cir_arc.normalAt(obj.t).normalize()
81
82                  # points for the minor radius of the ellipse
83      minor_rad_p1 = FreeCAD.Vector(normal_dir_cen_ell.multiply(obj.t/2))+
    ell_cen
84      minor_rad_p2 = ell_cen-FreeCAD.Vector(normal_dir_cen_ell)
85
86      # this is the elliptical arc that forms the leading edge
87      ell_leading_edge = Part.ArcOfEllipse(Part.Ellipse(intersect_le_point,
        minor_rad_p2, ell_cen), -pi/2, pi/2).toShape()
88
89      # edge on the suction side
90      ell_leading_edge_vertex0 = ell_leading_edge.Vertexes[0].Point
91
92      # edge on the pressure side
93      ell_leading_edge_vertex1 = ell_leading_edge.Vertexes[1].Point
94      #Part.show(ell_leading_edge)
95
96      # this is the point on the camber line (circular arc) that that will
    be used to delineate the suction and pressure sides of the blade
97      p1_cl = cir_arc.valueAt(cir_arc.getParameterByLength(0.5*cir_arc.
    Length))
98
99      # normal direction to the camber line towards the suction side at the
        point established at the last line of code
100     tangent_p1_cl = (cir_arc.valueAt(cir_arc.getParameterByLength(0.5*
    cir_arc.Length))-cir_arc.valueAt(cir_arc.getParameterByLength(0.49*
    cir_arc.Length))).normalize()

101     tangent_point1 = FreeCAD.Vector(tangent_p1_cl.multiply(obj.t/2))+
    p1_cl
102     tangent_line1 = Part.LineSegment(p1_cl, tangent_point1).toShape()
103     tangent_line1.rotate(p1_cl, FreeCAD.Vector(1, 0, 0), 90)
104     #Part.show(tangent_line1)
105
```

```
106     # normal direction to the camber line towards the pressure side at
    the point p1_cl
107     tangent_point2 = FreeCAD.Vector(tangent_p1_cl)+p1_cl
108     tangent_line2 = Part.LineSegment(p1_cl, tangent_point2).toShape()
109     tangent_line2.rotate(p1_cl, FreeCAD.Vector(1, 0, 0), -90)
110     #Part.show(tangent_line2)
111 
112     # this is another point on the camber line (circular arc) that that
    will be used to delineate the both sides of the blade
113     p2_cl = cir_arc.valueAt(cir_arc.getParameterByLength(cir_arc.Length))
114 
115     # normal direction to the camber line towards the suction side at the
     point established at the last line of code
116     tangent_p2_cl = (cir_arc.valueAt(cir_arc.getParameterByLength(cir_arc
    .Length))-cir_arc.valueAt(cir_arc.getParameterByLength(0.99*cir_arc.
    Length))).normalize()

117     tangent_point3 = FreeCAD.Vector(tangent_p2_cl.multiply(obj.t/2))+
    p2_cl
118     tangent_line3 = Part.LineSegment(p2_cl, tangent_point3).toShape()
119     tangent_line3.rotate(p2_cl, FreeCAD.Vector(1, 0, 0), 90)
120     #Part.show(tangent_line3)
121 
122     # normal direction to the camber line towards the pressure side at
    the point p2_cl
123     tangent_point4 = FreeCAD.Vector(tangent_p2_cl)+p2_cl
124     tangent_line4 = Part.LineSegment(p2_cl, tangent_point4).toShape()
125     tangent_line4.rotate(p2_cl, FreeCAD.Vector(1, 0, 0), -90)
126     #Part.show(tangent_line4)
127 
128     # Pressure side delineated as circular arc (extended to about the
    last vertex of the outlet construction line)
129     cir_arc_ps_dummy = Part.Arc(ell_leading_edge_vertex1, tangent_line2.
    Vertexes[1].Point, tangent_line4.Vertexes[1].Point).toShape()
130     #Part.show(cir_arc_ps_dummy)
131 
132     # the intersection of the arc established on the pressure side with
    the outlet construction circle will form a vertex of the trailing
    edge
133     intersect_te_ps = cir_arc_ps_dummy.Curve.intersect(circle_out_cons.
    Curve)[0].toShape().Point
134 
135     # the intersecting point established can now be used to delineate the
     pressure part of the blade the estends only until the outlet
    construction line
```

```
136     cir_arc_ps = Part.Arc(ell_leading_edge_vertex1, tangent_line2.
    Vertexes[1].Point, intersect_te_ps).toShape()
137
138     # Need to make sure the right intersection point is being used for
    blade profiling
139     if cir_arc_ps.Length > cir_arc_ps_dummy.Length:
140       intersect_te_ps = cir_arc_ps_dummy.Curve.intersect(circle_out_cons.
    Curve)[1].toShape().Point
141       cir_arc_ps = Part.Arc(ell_leading_edge_vertex1, tangent_line2.
    Vertexes[1].Point, intersect_te_ps).toShape()
142     #Part.show(cir_arc_ps)
143
144     # Suction side delineated as circular arc (extended to the outlet
    construction line)
145     cir_arc_ss_dummy = Part.Arc(ell_leading_edge_vertex0, tangent_line1.
    Vertexes[1].Point, tangent_line3.Vertexes[1].Point).toShape()
146     #Part.show(cir_arc_ss_dummy)
147
148     # the intersection of the arc established on the suction side with
    the outlet construction circle will form a vertex of the trailing
    edge
149     intersect_te_ss = cir_arc_ss_dummy.Curve.intersect(circle_out_cons.
    Curve)[0].toShape().Point
150
151     # Pressure side delineated as circular arc (extended to the outlet
    construction line)
152     cir_arc_ss = Part.Arc(ell_leading_edge_vertex0, tangent_line1.
    Vertexes[1].Point, intersect_te_ss).toShape()
153
154     # Need to make sure the right intersection point is being used for
    blade profiling
155     if cir_arc_ss.Length > cir_arc_ss_dummy.Length:
156       intersect_te_ss = cir_arc_ss_dummy.Curve.intersect(circle_out_cons.
    Curve)[1].toShape().Point
157       cir_arc_ss = Part.Arc(ell_leading_edge_vertex0, tangent_line1.
    Vertexes[1].Point, intersect_te_ss).toShape()
158     #Part.show(cir_arc_ss)
159
160     # trailing edge as a simple straight line segment
161     te_line = Part.LineSegment(intersect_te_ps, intersect_te_ss).toShape
    ()
162
163     # blade plane as a face
164     blade_wire = Part.Wire([ell_leading_edge, cir_arc_ss, te_line,
    cir_arc_ps], closed = True)
```

```
    blade_face = Part.Face(blade_wire)
    #Part.show(blade_wire)

    # extrusion of blade face to form a 3D blade solid
    blade_solid1 = blade_face.extrude(App.Vector(obj.b, 0, 0))
    blade_solid2 = blade_face.extrude(App.Vector(-obj.b, 0, 0))
    blade_solid = Part.Compound([blade_solid1, blade_solid2])

    # extrusion of blade wire to form a 3D blade surface
    blade_surface1 = blade_wire.extrude(App.Vector(obj.b, 0, 0))
    blade_surface2 = blade_wire.extrude(App.Vector(-obj.R3, 0, 0))
    blade_surface = Part.Compound([blade_surface1, blade_surface2])
    #Part.show(blade_surface)

    # array of the blades (solids)
    no_blades = int(obj.Z)
    Angle_rotation_blade = 360./float(obj.Z)
    blades_solid = []
    for i in range (0, no_blades, 1):
      blade_solid_i = blade_solid.copy()
      blade_solid_i.rotate(FreeCAD.Vector(0, 0, 0), FreeCAD.Vector(1, 0,
0), Angle_rotation_blade*(i))
      blades_solid.append(blade_solid_i)

    # creation of points defining the meridional plane of the impeller

    # creation of points defining the shroud
    shroudP1 = FreeCAD.Vector(obj.L0, obj.R1, 0)
    shroudP2 = FreeCAD.Vector(obj.L0+obj.L1, obj.R1, 0)
    shroudP3 = FreeCAD.Vector(obj.L0+obj.L1+obj.R3, obj.R1+obj.R3, 0)
    shroudP4 = FreeCAD.Vector(obj.L0+obj.L1+obj.R3, obj.R0, 0)

    # the points below are used to create the circular arc used to join
the horizontal and vertical line segments of the shroud profile
    shroud_cons_1 = FreeCAD.Vector(obj.L0+obj.L1, obj.R1+obj.R3, 0)
    shroud_cons_2 = FreeCAD.Vector(obj.L0+obj.L1, obj.R1+obj.R3+obj.R3,
0)

    # creation of points defining the hub
    hubP1 = FreeCAD.Vector(obj.L0, obj.R2, 0)
    hubP2 = FreeCAD.Vector(obj.L0+obj.L1, obj.R2, 0)
    hubP3 = FreeCAD.Vector(obj.L0+obj.L1+obj.R3+obj.b, obj.R1+obj.R3, 0)
    hubP4 = FreeCAD.Vector(obj.L0+obj.L1+obj.R3+obj.b, obj.R0, 0)

    # the point below is used to create a B-spline curve used to join the
```

```
    horizontal and vertical line segments of the hub profile
    hub_cons = FreeCAD.Vector(obj.L0+obj.L1+obj.R3+obj.b, obj.R2, 0)

    # shroud profile created as a wire joining 2 line segments and a
    circular arc
    shroud_profile_1 = Part.LineSegment(shroudP1,shroudP2).toShape()
    shroud_circle = Part.Circle(shroudP2, shroudP3, shroud_cons_2)
    shroud_profile_2 = Part.Arc(shroud_circle, 0, pi/2).toShape()
    shroud_profile_3 = Part.LineSegment(shroudP3,shroudP4).toShape()
    shroud_wire = Part.Wire([shroud_profile_1, shroud_profile_2,
    shroud_profile_3])
    shroud_surface = shroud_wire.revolve(FreeCAD.Vector(0,0,0), FreeCAD.
    Vector(1,0,0), 360)
    shroud_surface_cut = shroud_surface.cut(Part.Compound(blades_solid))
    #Part.show(shroud_surface_cut)

    # hub profile created as a wire
    hub_profile_1 = Part.LineSegment(hubP1, hubP2).toShape()
    hub_profile_2_cons = Part.BSplineCurve([hubP3, hub_cons, hubP2],None,
    None,False,3,None,False)
    hub_profile_2 = Part.Edge(hub_profile_2_cons)
    hub_profile_3 = Part.LineSegment(hubP3, hubP4).toShape()
    hub_wire = Part.Wire([hub_profile_1, hub_profile_2, hub_profile_3])
    hub_surface = hub_wire.revolve(FreeCAD.Vector(0,0,0), FreeCAD.Vector
    (1,0,0), 360)
    hub_surface_cut = hub_surface.cut(Part.Compound(blades_solid))
    #Part.show(hub_surface_cut)

    # creation of interface between impeller and inlet pipe
    imp_inl_interface2D = Part.LineSegment(shroudP1,hubP1).toShape()
    imp_inl_interface = imp_inl_interface2D.revolve(FreeCAD.Vector(0,0,0)
    , FreeCAD.Vector(1,0,0), 360)

    # creation of interface between impeller and volute_pipe
    imp_vol_interface2D = Part.LineSegment(shroudP4, hubP4).toShape()
    imp_vol_interface = imp_vol_interface2D.revolve(FreeCAD.Vector(0,0,0)
    , FreeCAD.Vector(1,0,0), 360)

    # creation of the solids outside the impeller to cut through blade
    surface extruded using wires that will delineate the blade surface
    inside the impeller domain
    # solid outside the shroud side
    shroudP5 = FreeCAD.Vector(obj.L0+obj.L1, obj.R0, 0)
    shroud_profile_4 = Part.LineSegment(shroudP4, shroudP5).toShape()
    shroud_profile_5 = Part.LineSegment(shroudP5, shroudP2).toShape()
```

```
242     shroud_wire_2 = Part.Wire([shroud_profile_2, shroud_profile_3,
    shroud_profile_4, shroud_profile_5], closed = True)
243     shroud_face_outside = Part.Face(shroud_wire_2)
244     shroud_solid_outside =  shroud_face_outside.revolve(FreeCAD.Vector
    (0,0,0), FreeCAD.Vector(1,0,0), 360)
245 
246     # solid outside the hub side
247     hubP5 = FreeCAD.Vector(obj.L0+obj.L1+obj.R3+obj.b, obj.R2, 0)
248     hub_profile_4 = Part.LineSegment(hubP3, hubP5).toShape()
249     hub_profile_5 = Part.LineSegment(hubP5, hubP2).toShape()
250     hub_wire_2 = Part.Wire([hub_profile_2, hub_profile_4, hub_profile_5],
     closed = True)
251     hub_face_outside = Part.Face(hub_wire_2)
252     hub_solid_outside = hub_face_outside.revolve(FreeCAD.Vector(0,0,0),
    FreeCAD.Vector(1,0,0), 360)
253 
254     imp_outside_solid = Part.Compound([shroud_solid_outside,
    hub_solid_outside])
255     #Part.show(imp_outside_solid)
256 
257     # array of the blades (surfaces)
258     no_blades = int(obj.Z)
259     Angle_rotation_blade = 360./float(obj.Z)
260     blades_surface = []
261     for i in range (0, no_blades, 1):
262       blade_surface_i = blade_surface.copy()
263       blade_surface_i.rotate(FreeCAD.Vector(0, 0, 0), FreeCAD.Vector(1,
    0, 0), Angle_rotation_blade*(i))
264       blade_i = blade_surface_i.cut(imp_outside_solid)
265       blades_surface.append(blade_i)
266 
267     blades_compound = Part.Compound(blades_surface)
268     #Part.show(blades_compound)
269 
270     # exporting the impeller geometry
271     imp_stls = [imp_inl_interface, imp_vol_interface, shroud_surface_cut,
     hub_surface_cut, blades_compound]
272     imp_stls_names = ["inlet_impeller_interface", "
    impeller_volute_interface", "shroud", "hub", "blades"]
273 
274     for i,fig in enumerate(imp_stls):
275       fig.exportStl(export_dir_imp + imp_stls_names[i] + ".stl")
276 
277     # creating the inlet pipe
278     inletP1 = FreeCAD.Vector(0, obj.R2, 0)
```

```
    inletP2 = FreeCAD.Vector(0, obj.R1, 0)

    # surfaces defining the inlet pipe
    inlet_line = Part.LineSegment(inletP2, inletP1).toShape()
    inlet = inlet_line.revolve(FreeCAD.Vector(0,0,0), FreeCAD.Vector
    (1,0,0), 360)

    inlet_pipe_line = Part.LineSegment(shroudP1, inletP2).toShape()
    inlet_pipe = inlet_pipe_line.revolve(FreeCAD.Vector(0,0,0), FreeCAD.
    Vector(1,0,0), 360)

    shaft_line = Part.LineSegment(inletP1, hubP1).toShape()
    shaft = shaft_line.revolve(FreeCAD.Vector(0,0,0), FreeCAD.Vector
    (1,0,0), 360)

    # exporting the inlet pipe geometry
    inlet_stls = [inlet, inlet_pipe, shaft, imp_inl_interface]
    inlet_stls_names = ["inlet", "inlet_pipe", "shaft", "
    inlet_impeller_interface"]
    for i,fig in enumerate(inlet_stls):
      fig.exportStl(export_dir_inlet + inlet_stls_names[i] + ".stl")

    # creating the volute goemetry

    shroud_thickness_cons_line = Part.LineSegment(FreeCAD.Vector(obj.L0+
    obj.L1+obj.R3, obj.R0, 0), FreeCAD.Vector(obj.L0+obj.L1+obj.R3-obj.L3
    , obj.R0, 0)).toShape()
    shroud_thickness = shroud_thickness_cons_line.revolve(FreeCAD.Vector
    (0,0,0), FreeCAD.Vector(1,0,0), 360)

    hub_thickness_cons_line = Part.LineSegment(FreeCAD.Vector(obj.L0+obj.
    L1+obj.R3+obj.b, obj.R0, 0), FreeCAD.Vector(obj.L0+obj.L1+obj.R3+obj.
    b+obj.L3, obj.R0, 0)).toShape()
    hub_thickness = hub_thickness_cons_line.revolve(FreeCAD.Vector(0,0,0)
    , FreeCAD.Vector(1,0,0), 360)

    # creation of the points defining the volute front surface
    p_throat = FreeCAD.Vector(obj.L0+obj.L1+obj.R3-obj.L3, obj.R0+obj.L5+
    obj.L4, 0)
    p_75throat = FreeCAD.Vector(obj.L0+obj.L1+obj.R3-obj.L3, 0, obj.R0+
    obj.L6+obj.L4)
    p_50throat = FreeCAD.Vector(obj.L0+obj.L1+obj.R3-obj.L3, -(obj.R0+obj
    .L7+obj.L4), 0)
    p_25throat = FreeCAD.Vector(obj.L0+obj.L1+obj.R3-obj.L3, 0, -(obj.R0+
    obj.L8+obj.L4))
```

```
310
311     # creation of cutwater
312     # the first two points create the line the will be rotated to define
    the position of cutwater
313     p1_cutwater = FreeCAD.Vector(obj.L0+obj.L1+obj.R3-obj.L3, 0, 0)
314     p2_cutwater = FreeCAD.Vector(obj.L0+obj.L1+obj.R3-obj.L3, obj.R0+obj.
    L4, 0)
315     line_cutwater = Part.LineSegment(p1_cutwater, p2_cutwater).toShape()
316     line_cutwater.rotate(p1_cutwater, FreeCAD.Vector(1, 0, 0), 360 - obj.
    theta_3)
317     p3_cutwater = line_cutwater.Vertexes[1].Point
318     p4_cutwater = FreeCAD.Vector(p3_cutwater.x, p3_cutwater.y+obj.R4,
    p3_cutwater.z)
319     # the factor of 1.03285 in the line of code below is hard-coded. This
        is to endure that the circular arc of the cutwater is tangent to the
        spiral volute
320     p5_cutwater = FreeCAD.Vector(p3_cutwater.x, p3_cutwater.y+obj.R4/2,
    p3_cutwater.z+obj.R4/2-1.03285)
321     cutwater_profile = Part.Arc(p3_cutwater, p5_cutwater, p4_cutwater).
    toShape()
322
323     # creation of arcs defining the volute front wall
324     vol_arc1 = Part.Arc(p_throat, p_75throat, p_50throat).toShape()
325     vol_arc2 = Part.Arc(p_50throat, p_25throat, p3_cutwater).toShape()
326
327     # creation of the lines and points defining the diffuser front
    surface
328     p1_outlet = FreeCAD.Vector(p_throat.x, p_throat.y, p_throat.z-obj.L9)
329     p2_outlet = FreeCAD.Vector(p_throat.x, p4_cutwater.y, p1_outlet.z)
330     outlet_l1 = Part.LineSegment(p_throat, p1_outlet).toShape()
331     outlet_l2 = Part.LineSegment(p1_outlet, p2_outlet).toShape()
332     outlet_l3 = Part.LineSegment(p2_outlet, p4_cutwater).toShape()
333
334     # creation of the circle that defines the outer outlines of shroud
    and hub
335     shroud_outer_outline = Part.Circle(FreeCAD.Vector(p_throat.x, 0, 0),
    FreeCAD.Vector(1, 0, 0), obj.R0).toShape()
336     hub_outer_outline = Part.Circle(FreeCAD.Vector(p_throat.x + obj.b +
    2*obj.L3, 0, 0), FreeCAD.Vector(1, 0, 0), obj.R0).toShape()
337
338     # creating volute surfaces from arc and line segments
339
340     # volute front face
341     vol_wire1 = Part.Wire([vol_arc1, vol_arc2, cutwater_profile,
    outlet_l3, outlet_l2, outlet_l1])
```

```
342     vol_face_front = Part.Face([vol_wire1, shroud_outer_outline], "Part::
    FaceMakerBullseye")
343 
344     # volute extrusion
345     vol_wire2 = Part.Wire([vol_arc1, vol_arc2, cutwater_profile,
    outlet_l3, outlet_l1])
346     vol_extrusion = vol_wire2.extrude(App.Vector(obj.b + 2*obj.L3, 0, 0))
347 
348     # volute back surface
349     vol_wire3 = Part.Wire([vol_arc1, vol_arc2, cutwater_profile,
    outlet_l3, outlet_l2, outlet_l1])
350     vol_wire3.translate(App.Vector(obj.b + 2*obj.L3, 0, 0))
351     vol_face_back = Part.Face([vol_wire3, hub_outer_outline], "Part::
    FaceMakerBullseye")
352     #Part.show(vol_face_front)
353     #Part.show(vol_extrusion)
354     #Part.show(vol_face_back)
355 
356     # outlet face
357     outlet_face = outlet_l2.extrude(App.Vector(obj.b + 2*obj.L3, 0, 0))
358     #Part.show(outlet_face)
359 
360     # exporting the volute geometry
361     volute_stls = [imp_vol_interface, shroud_thickness, hub_thickness,
    vol_face_front, vol_extrusion, vol_face_back, outlet_face]
362     volute_stls_names = ["volute_impeller_interface", "shroud_thickness"
    , "hub_thickness", "volute_front_face", "volute_extrusion", "
    volute_back_face", "outlet"]
363 
364     for i,fig in enumerate(volute_stls):
365       fig.exportStl(export_dir_volute + volute_stls_names[i] + ".stl")
366 
367 
368 
369 doc = FreeCAD.newDocument()
370 myObj = doc.addObject("Part::FeaturePython","Pump")
371 Pump(myObj)
372 Pump.execute(Pump,myObj)
373 #myObj.ViewObject.Proxy = 0 # this is mandatory unless we code the
    ViewProvider too
```

Appendix B

Turbulence Models

B.1 k-ε Model

The turbulent viscosity is evaluated using equation:

$$v_t = \beta^* \frac{k^2}{\epsilon} \tag{B.1}$$

where k is the Turbulent Kinetic Energy (TKE), ϵ is the turbulent dissipation rate, and β^* is the empirical constant. The equations used to define the variables k and ϵ are defined as:

$$\begin{aligned} \frac{\partial (U_i k)}{\partial x_j} &= \frac{\partial \left(\frac{v_t}{\sigma_k} \frac{\partial k}{\partial x_j} \right)}{\partial x_j} + P_k - \epsilon \\ \frac{\partial (U_j \epsilon)}{\partial x_j} &= \frac{\partial \left(\frac{v_t}{\sigma_\epsilon} \frac{\partial \epsilon}{\partial x_j} \right)}{\partial x_j} + \frac{\epsilon}{k} (C_{\epsilon 1} P_k - C_{\epsilon 2} \epsilon) \end{aligned} \tag{B.2}$$

where σ_k, σ_ϵ, $C_{\epsilon 1}$, and $C_{\epsilon 2}$ are empirical constants, while P_k is the rate of generation of TKE defined as:

$$P_k = -\overline{u_i u_j} \frac{\partial U_i}{\partial x_j} \tag{B.3}$$

In equation (B.3), the term $\overline{u_i u_j}$ is an important term in turbulence modelling, referred to as Reynolds-stress tensor. It is defined as:

$$\overline{u_i u_j} = \frac{2}{3} \delta_{ij} k - v_t \left(\frac{\partial U_i}{\partial x_j} + \frac{\partial U_j}{\partial x_i} \right) \tag{B.4}$$

B.2 k-ω Model

In the $k-\omega$ model, the turbulent viscosity for stress tensor is determined using:

$$v_t = \frac{k}{\omega} \tag{B.5}$$

where ω is referred to as the turbulent frequency. The two quantities, k and ω, in this model are determined using:

$$\begin{aligned} \frac{\partial\left(U_j k\right)}{\partial x_j} &= \frac{\partial\left(\left(v+\frac{v_t}{\sigma_k}\right)\frac{\partial k}{\partial x_j}\right)}{\partial x_j} + P_k - \beta' k\omega \\ \frac{\partial\left(U_j \omega\right)}{\partial x_j} &= \frac{\partial\left(\left(v+\frac{v_t}{\sigma_\omega}\right)\frac{\partial \omega}{\partial x_j}\right)}{\partial x_j} + \alpha\frac{\omega}{k}P_k - \beta_1\omega^2 \end{aligned} \tag{B.6}$$

where β', β_1, σ_k, α, and σ_ω are empirical constants. The $k-\omega$ is particularly beneficial for near-wall treatment. This is in contrast to the standard $k-\epsilon$ model that requires the damping functions and much finer near-wall resolution for wall treatment.

B.3 SST k-ω Model

The SST $K-\omega$ model combines the $k-\epsilon$ and $k-\omega$ models, which involves the use of the blending function F_1. The model $k-\omega$ is multiplied by F_1, and the model $k-\epsilon$ by $1-F_1$. The blending function, F_1, is defined as:

$$F_1 = \tanh\left(\arg_1^4\right) \tag{B.7}$$

where $\arg_1$ is defined as:

$$\arg_1 = \min\left(\max\left(\frac{\sqrt{k}}{\beta'\omega y}, \frac{500v}{y^2\omega}\right), \frac{4\rho k}{CD_{k\omega}\sigma_{\omega 2} y^2}\right) \tag{B.8}$$

.

In equation (B.8), $\sigma_{\omega 2}$ is an empirical constant, y is the smallest distance to the wall, and $CD_{k\omega}$ is defined as:

$$CD_{k\omega} = \max\left(2\rho\frac{1}{\sigma_{\omega 2}\omega}\frac{\partial k}{\partial x_j}\frac{\partial \omega}{\partial x_j}, 10^{-10}\right) \tag{B.9}$$

.

The turbulent viscosity for this model is evaluated using:

$$v_t = \frac{\alpha_1 k}{\max\left(\alpha_1 \omega, SF_2\right)} \tag{B.10}$$

where α_1 is an empirical constant, S is the strain rate, and F_2 is another blending function used as a correction for free shear flows. It is defined as:

$$F_2 = \tanh\left(\arg_2^2\right) \tag{B.11}$$

where $\arg_2$ is defined using:

$$\arg_2 = \max\left(\frac{2\sqrt{k}}{\beta' \omega y}, \frac{500v}{y^2 \omega}\right) \tag{B.12}$$

Appendix C

Mesh used for Numerical Simulations

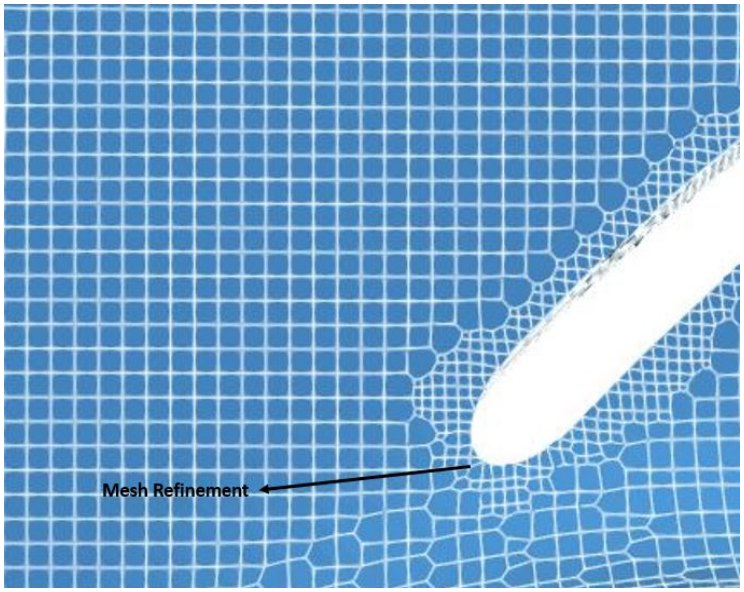

Figure C.1: Mesh refinement at the impeller inlet

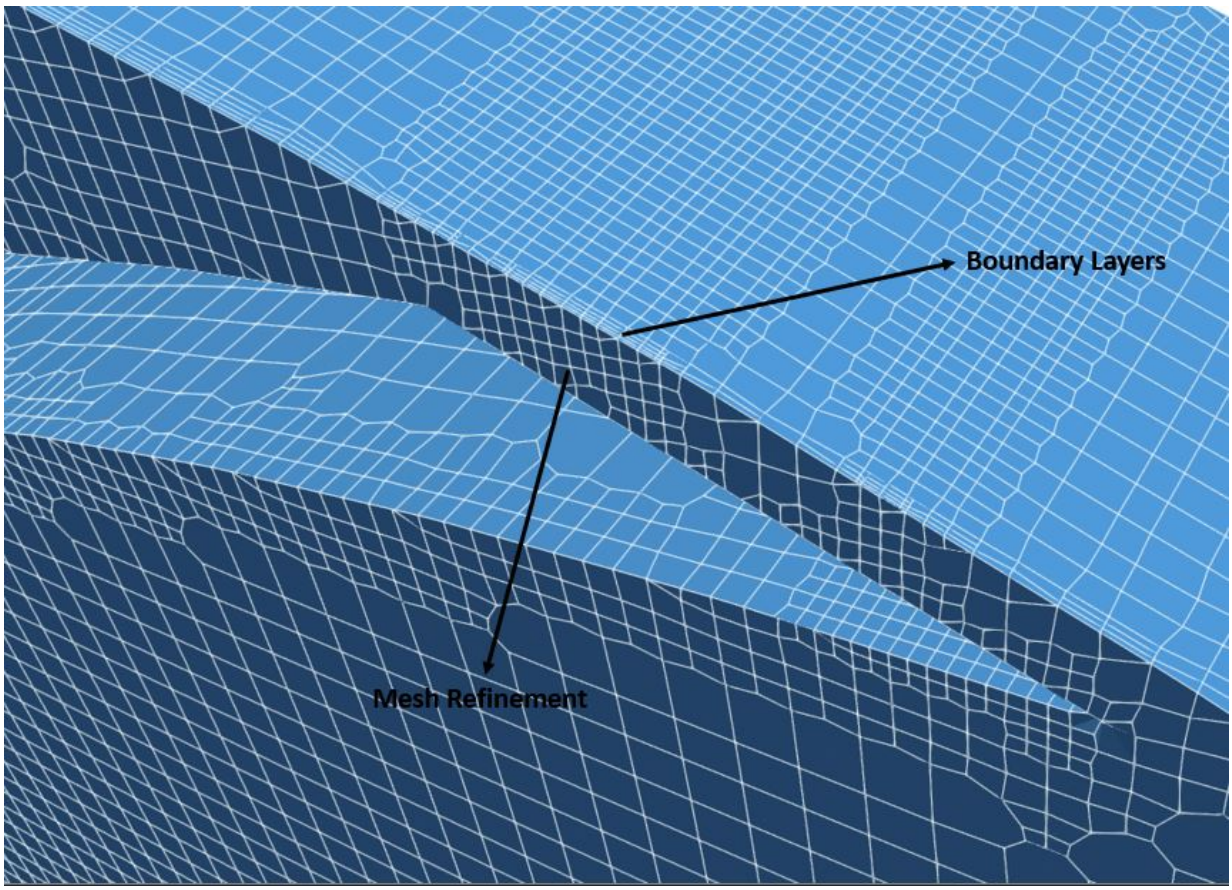

Figure C.2: Mesh refinement at the impeller outlet

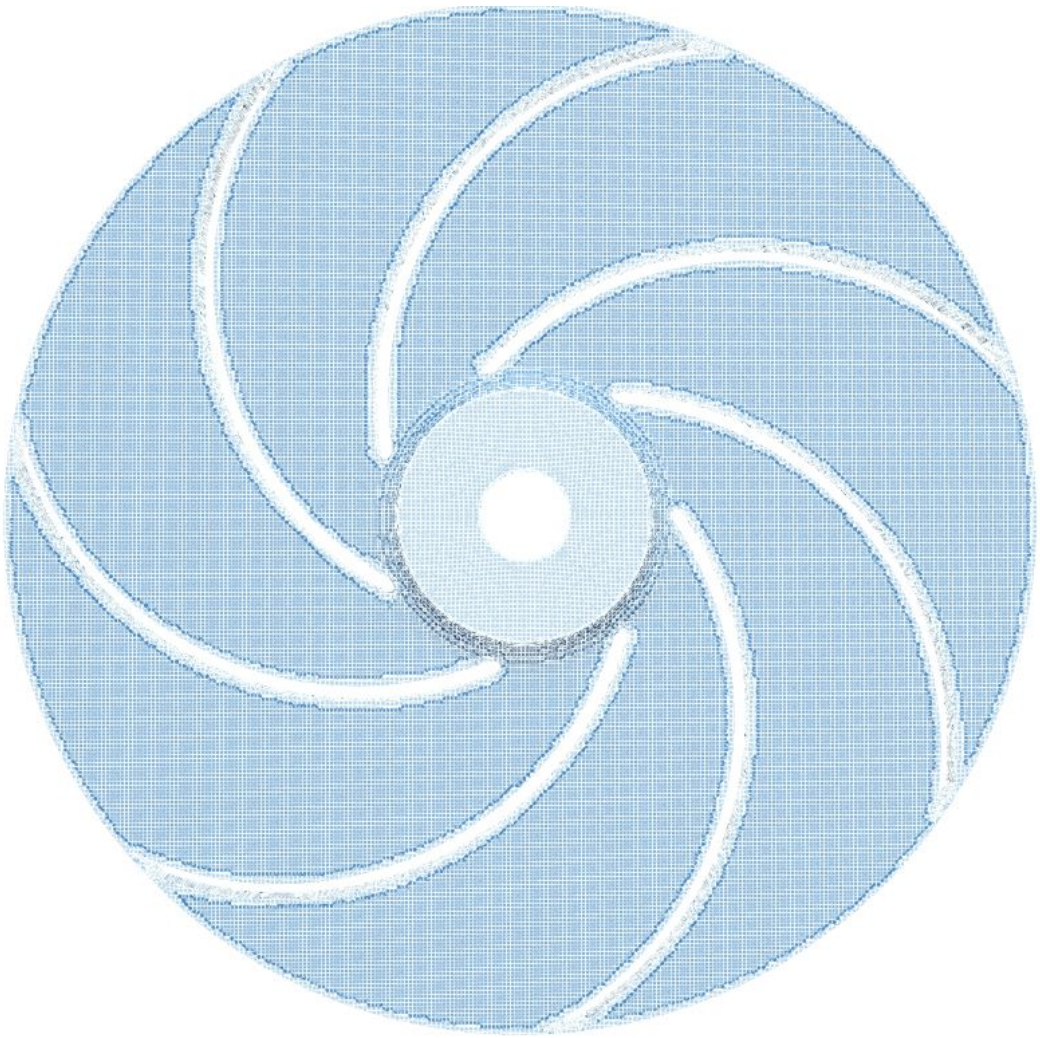

Figure C.3: Mesh for the impeller

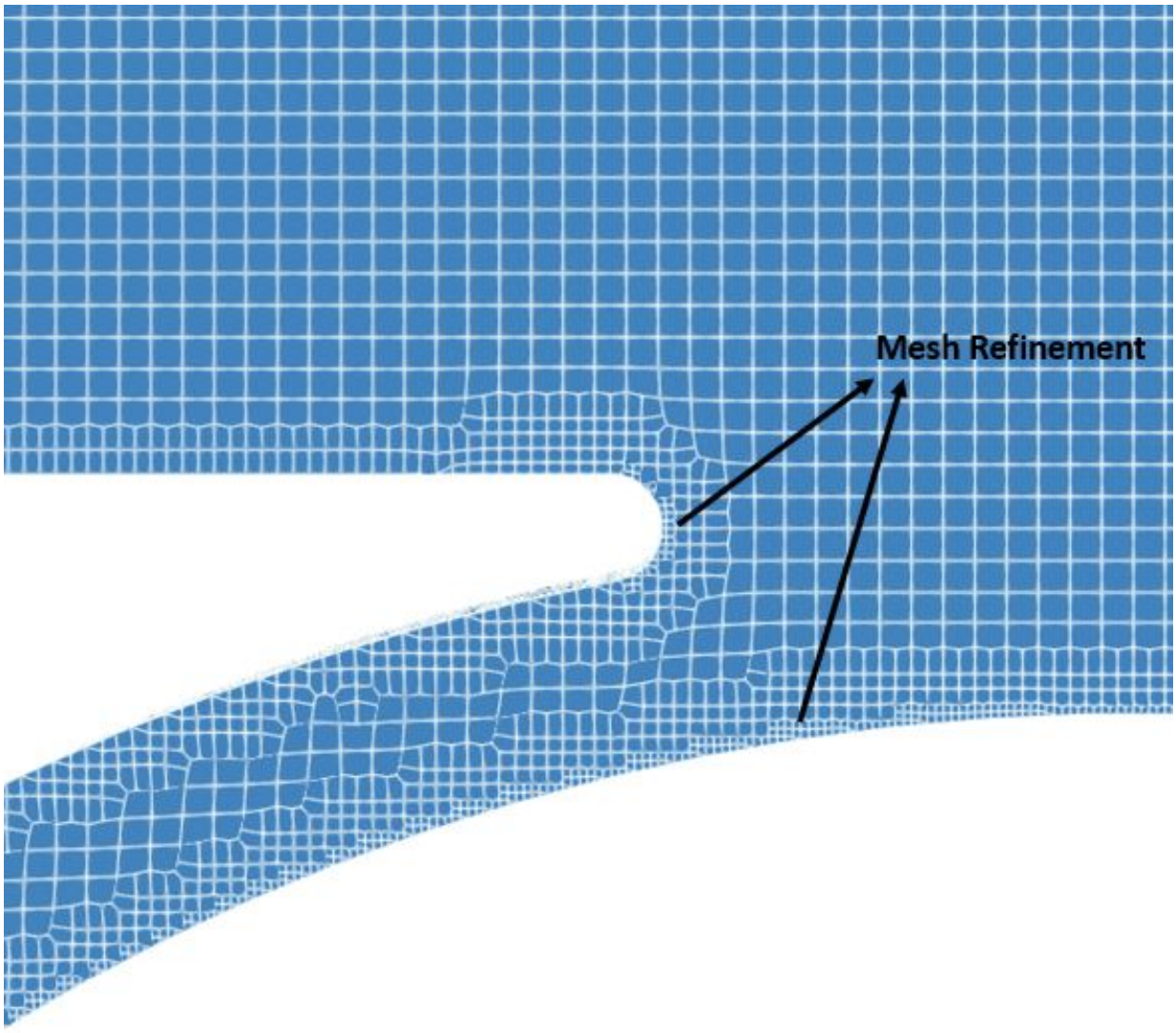

Figure C.4: Mesh refinement near the tongue of the volute

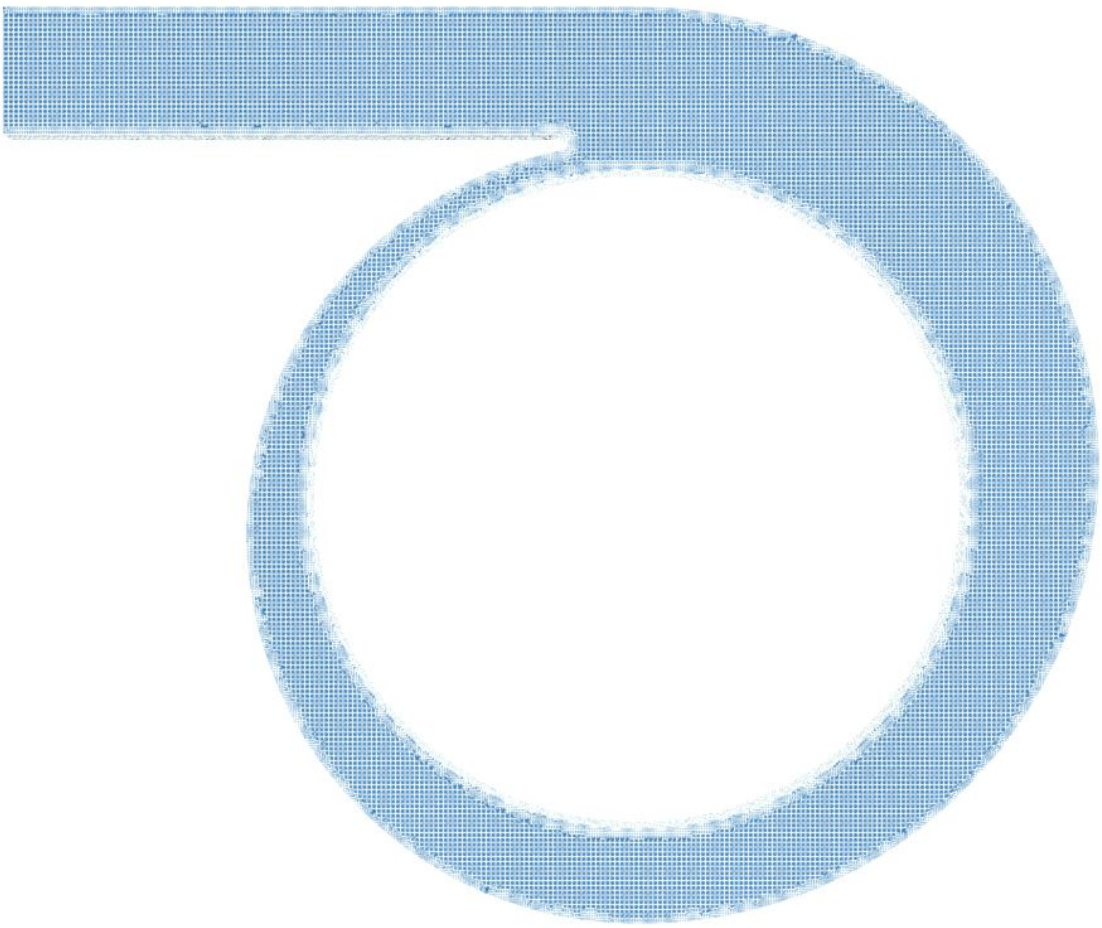

Figure C.5: Mesh for the volute